Photocatalytic Hydrogen Peroxide Production by Antimony- and Potassium-Doped Polymeric Carbon Nitride

Tobias Nikolajsen Kudahl
9-10TH semester
Aalborg University

Department of Chemistry and Bioscience
Frederik Bajers Vej 7H
9220 Aalborg Ø
www.bio.aau.dk

AALBORG UNIVERSITY
STUDENT REPORT

Title:

Photocatalytic Hydrogen Peroxide Production by Antimony- and Potassium-Doped Polymeric Carbon Nitride

Project:

9-10th semester project

Project Period:

1st September 2024 - 22nd December 2025

Participants:

Tobias Nikolajsen Kudahl

Supervisors:

Vittorio Boffa - Associate Professor
Jingbo Ni - Post. Doc

Number of Pages: 65
Date of completion: 22nd December 2025

Abstract

This project seeks to investigate polymeric carbon nitride as a promosing photocatalyst for sustainable hydrogen peroxide production. In this work, PCN was systematically doped through single and co-doping with antimony and potassium to enhance its photocatalytic activity. Characterization techniques such as X-ray diffraction, Fourier-transform infrared spectroscopy, X-ray photoelectron spectroscopy, UV–Vis spectroscopy, photoluminescence (PL), time-resolved photoluminescence, electron paramagnetic resonance, and electrochemical impedance spectroscopy, was used to evaluate the infleunce of dopant incorporation on the structure, optical, and electronic properties of polymeric carbon nitride.

The results confirmed successful Sb and K incorporation, while still maintaining the framework of polymeric carbon nitride. Doping induced a redshift in the absorption edge and a reduction in bandgap energy, which resulted in enhanced visible-light absorption. PL and TRPL analyses revealed suppressed charge recombination and improved charge-carrier dynamics, while EPR measurements indicated enhanced photoinduced charge activity and oxygen activation. EIS demonstrated a reduction in charge-transfer resistance for doped sample, particularly for K-doped and Sb-K doped PCN at optimal dopant ratios.

Photocatalytic experiment showed that Sb-doped PCN exhibit enhanced H_2O_2 generation compared to Pristine PCN with an optimal K and Sb loading of 1.25 mmol. Co-doping with potassium at low K concentration enhhanced the photocatalytic activity due to possible synergistic effects between electronic structure modulation and enhanced charge transport. Photocatalytic test with different pH conditions showed the acid and neutral environemnts favor H_2O_2 generation, whereas alkaline conditions suppress activity due to H_2O_2 instability.

Preface

This project is a one-year thesis project in Chemistry at Aalborg University. The project is a study of *Photalytic generation of hydrogen peroxide*. A prerequisite for reading the paper is the knowledge acquired from a BSc in chemisty. The help and funding from the two supervisors Vittorio Boffa and Jingbo Ni has been greatly appreciated in making the project.

Reading guide

The references in the project are made using the Vancouver system, and appear in chronological order in the report. The reference is placed at the end of sentence or paragraph where it refers to the preceding piece of text. The complete bibliography can be found at the end of the report, with the all references in chronological order of appearance.

References to figures, tables and equations appears with chapter number followed by the reference number for the chapter. Each figure and table have a caption withe additional information below or above respectively. The figures have been made by the authors unless otherwise specified. A list of the different abbreviations used can be seen after this chapter.

List of abbreviations

Abbreviation	Definition
UV-Vis DRS	Ultraviolet-Visible Diffuse Reflectance Spectroscopy
XRD	X-ray diffraction
XPS	X-ray photoelectron spectroscopy
FT-IR	Fourier Transform Infrared Spectroscopy
TRPL	Time-Resolved Photoluminescence
PL	Photoluminescence
EPR	Electron Paramagnetic Resonance
EIS	Electrochemical Impedance Spectroscopy
NHE	Normal Hydrogen Electrode
ORR	Oxygen Reduction Reaction
WOR	Water Oxidation Reaction
SAC	Single-Atom Catalysts
PCN	Polymeric carbon nitride
DMSO	5,5-Dimethyl-1-pyrroline N-oxide
TEMPO	2,2,6,6-Tetramethylpiperidine-1-oxyl
VB	Valence Band
CB	Conduction Band
SEMO	Scanning Electron Microscopy
DFT	Density Functional Theory

Table 1: List of abbreviations used in the report

Contents

1 Introduction

Hydrogen peroxide (H_2O_2) is a versatile chemical oxidant that can be used for disinfection, sterilization, bleaching, chemical synthesis, and even in fuel cells. H_2O_2 is produced by the anthraquinone autoxidation method [1] [2]. However, challenges with this process include high energy consumption, generation of toxic by-products, and multiple processing steps [3].

Therefore, researchers have been trying to develop a more efficient and sustainable method to produce H_2O_2. One of these methods for producing H_2O_2 is through photocatalysis from water and oxygen. Photocatalysis converts solar energy into chemical energy by a photocatalyst involving redox reactions [4]. Moreover, photocatalysis doesn't need additional chemicals and high temperatures to be performed, meanwhile, still producing high purity H_2O_2. Photocatalysis has been shown to be both a sustainable economically and environmentally friendly alternative compared to the anthraquinone method [5].

The goal of this study is to investigate metal doping of polymeric carbon nitride as a photocatalyst for the selective photocatalytic production of hydrogen peroxide.

2 | Photocatalytic Materials

This chapter presents the fundamental theoretical background required for the analysis and discussion of photocatalytic hydrogen peroxide production. The principles of photocatalysis, semiconductor electronic structure, and charge-transfer mechanisms are introduced, followed by a focused discussion on polymeric carbon nitride (PCN) photocatalysts and the role of elemental doping in tuning their photocatalytic performance.

2.1 Photocatalysis

Photocatalysis refers to the acceleration of a photochemical reaction in the presence of a solid material, known as a photocatalyst, which absorbs light and facilitates redox reactions without being consumed in the process. A photocatalyst is typically a semiconductor material that can absorb photons with energy equal to or greater than its bandgap, thereby generating charge carriers that drive chemical transformations at the catalyst surface [6].

2.2 Fundamental Principles of Photocatalysis

In photocatalysis, the photocatalyst is generally a solid semiconductor in contact with a liquid. Upon irradiation with light of sufficient energy, electrons are excited from the valence band (VB) to the conduction band (CB), leaving behind positively charged holes in the VB. This excitation process generates electron-hole pairs, commonly referred to as photogenerated charge carriers. A schematic illustration of a photocatalytic mechanism involved in H_2O_2 formation is shown in Figure 2.1 [7].

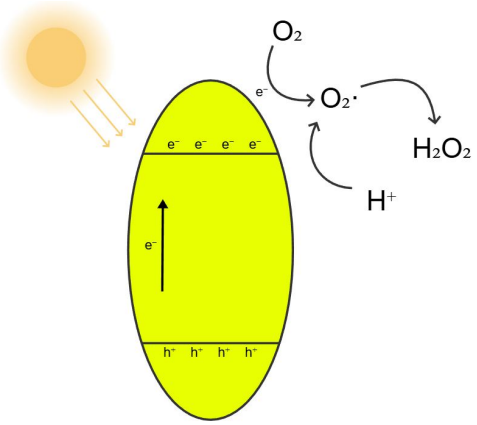

Figure 2.1: Schematic representation of the photocatalytic mechanism for H_2O_2 generation.

Following photoexcitation, two competing processes may occur. The excited electrons and holes can recombine, releasing the absorbed energy as heat or light and thereby reducing photocatalytic

efficiency. Alternatively, the charge carriers can migrate to the surface of the photocatalyst, where electrons participate in reduction reactions and holes drive oxidation reactions. The overall photocatalytic performance is therefore controlled by the efficiency of charge separation, transport, and surface reaction kinetics [7].

2.3 PCN

PCN is a promising photocatalyst that is a conjugated polymer composed of carbon and nitrogen linked through sp^2-hybridized C-N bonds, forming an extended π-conjugated framework based primarily on heptazine units. This conjugated structure enables charge delocalization within the planes [1]. The layered structure of PCN is stabilized by van der Waals interactions between the conjugated planes [8]. Additionally, it also exhibits an absorption at 460 nm and has a band gap of approximately 2.7 eV, which enables visible-light absorption [9].

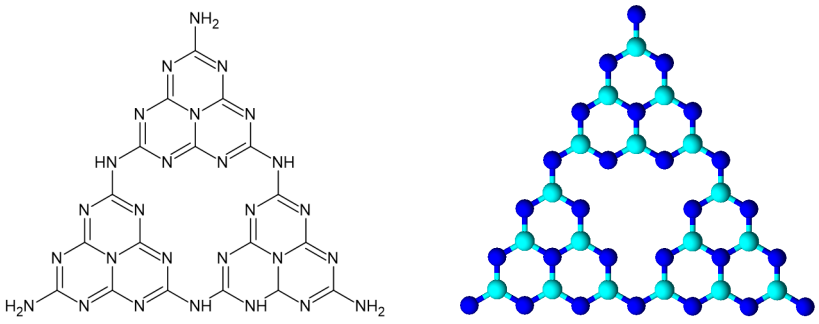

(a) 2D Stick Structure **(b)** 3D Ball Structure

Figure 2.2: Molecular Structure of three connected tri-s-heptazine units in a PCN network

The ideal structure of PCN primarily consists of carbon-nitrogen (C-N) bonds. Hydrogen is also present, mainly as primary -(NH_2) and secondary -(NH) amine groups at the terminal edges. However, the actual structure often deviates from this ideal due to incomplete heptazine units, resulting in the presence of cyanamide and various oxygen-containing functional groups, which can significantly impact catalytic activity. The formation of cyanamide may occur during the initial synthesis due to incomplete formation of heptazine or through thermal depolymerization processes [10].

2.3.1 Redox Thermodynamics and Band-Edge Alignment

The possibility of photocatalytic redox reactions is determined by the relative positions of the semiconductor band edges with respect to the redox potentials of the specific reactions. For a reduction reaction to proceed, the conduction band minimum must be more negative than the corresponding reduction potential, while oxidation reactions require the valence band maximum to be more positive than the oxidation potential [7].

PCN typically exhibits a conduction band minimum at approximately -1.1 to -1.3 V versus the normal hydrogen electrode (NHE) and a valence band maximum at around $+1.4$ V versus NHE, corresponding to

a band gap of approximately 2.7 eV [9, 1]. These band-edge positions makes PCN thermodynamically capable of reducing O_2 to H_2O_2 via the $2\,e^-$ oxygen reduction reaction (ORR), while also providing sufficient oxidative potential for water oxidation reduction (WOR) [11].

However, although both oxygen reduction and water oxidation are thermodynamically allowed, their kinetics and selectivity differ significantly. In particular, the strong oxidizing power of photogenerated holes is a risk for undesired oxidation or decomposition of H_2O_2 from the reaction seen in Equation 2.1.

$$2\,H_2O_2 \longrightarrow 2\,H_2O + O_2 \tag{2.1}$$

Therefore, controlling charge-carrier separation and directing surface reaction pathways is critical for achieving selective H_2O_2 production.

2.3.2 Photocatalytic Pathways

Photocatalytic production of H_2O_2 typically proceeds via two pathways, which are $2\,e^-$ oxygen reduction reaction (ORR), as seen in Equation (2.3), or $2\,e^-$ water oxidation reaction (WOR), as seen in Equation (2.2) [11].

$$2\,H_2O \longrightarrow H_2O_2 + 2\,H^+ + 2\,e^- \quad (1.76\text{ V vs. NHE}) \tag{2.2}$$

$$O_2 + 2\,H^+ + 2\,e^- \longrightarrow H_2O_2 \quad (0.695\text{ V vs. NHE}) \tag{2.3}$$

Here, the ORR pathway can be be achieved through either the direct $2\,e^-$ reduction, (2.3), or two-step e^- O_2 reaction, as seen in Equation (2.4) and (2.5). Upon light absorption, photogenerated electrons in the conduction band interact with adsorbed O_2 to form superoxide radicals [12].

$$e^- + O_2 \longrightarrow O_2{}^{\bullet -} \quad (-0.33\text{ V vs. NHE}) \tag{2.4}$$

These superoxide radicals can then undergo protonation to form H_2O_2.

$$O_2{}^{\bullet -} + e^- + 2\,H^+ \longrightarrow H_2O_2 \quad (1.44\text{ V vs. NHE}) \tag{2.5}$$

However, light-driven WOR is difficult to achieve due to uphill highly oxidative thermodynamics and the instability of H_2O_2 due to its weak O–O bond, leading to the decomposition of H_2O_2 to O_2, as seen in Equation (2.1) [5].

On the other hand, the ORR pathway is a possibility with a photocatalyst with a conduction band more negative than 0.69 V, this is also supported by other studies showing promising results [1]. For the ORR to be able to occur, then O_2 is required. One of the pathways for oxygen to be introduced is by the $4\,e^-$ WOR, as seen in Equation 2.6.

$$2\,H_2O + 4\,h^+ \longrightarrow O_2 + 4\,H^+ \quad (1.23\,V\ vs.\ NHE) \tag{2.6}$$

However, this reaction have to occur simultaneously with the ORR, which is a challenge as $4\,e^-$ WOR is slow and has high activity energy, which will give H_2O_2 time to decompose. Therefore, it is common to use a sacrificial agent as an electron donor such as EtOH to help maintain charge separation required for ORR and prevent oxidative holes from attacking H_2O_2 [13].

2.3.3 Direct and Indirect Band Gaps

The optical absorption behavior of semiconductor photocatalysts is strongly influenced by the nature of their electronic band gap. Depending on the relative momentum of electrons at the valence band maximum and conduction band minimum, semiconductors can exhibit either a direct or an indirect band gap [14].

In a direct band gap semiconductor, the valence band maximum and conduction band minimum occur at the same crystal momentum, making it possible to transitions between these bands via photon absorption without any requirement for momentum change. This results in a strong optical absorption near the band edge. For indirect band gap semiconductors, then the momentum is different making, it necessary to involve a phonon to keep the momentum during optical transitions, which makes it harder for transitions to occur, which results in a weaker absorption near the band edge [14].

PCN synthesized with melamine typically results in the formation of g-C3N4. However, due to incomplete formation of the g-C3N4 structure, it is instead referred to as PCN. Due to g-C3N4's morphological variability, then it can exhibit both direct and indirect bandgap values depending on specific configurations [15]. Theoretical calculations further indicate that while monolayer carbon nitride structures may show direct bandgaps, stacking them into multilayers leads to indirect bandgaps, showing how layered interactions and structural disorder introduce indirect transition pathways [16].

It is essential to understand if its direct or indirect bandgap for interpreting the optical absorption spectra. In doped PCN systems, changes in structural order, electronic delocalization, and defect density can alter the relative contributions of direct and indirect bandgaps, thereby influencing charge-carrier generation and overall photocatalytic activity.

2.3.4 Selectivity in Oxygen Reduction Reactions

The availability and adsorption of molecular oxygen are critical factor for the efficiency of the oxygen reduction reaction (ORR) and, consequently, the yield of H_2O_2. Enhancing O_2 adsorption on the photocatalyst surface is therefore a key strategy to improve photocatalytic performance. One effective approach involves the introduction of single-atom catalysts (SACs), which are typically isolated metal atoms anchored to the PCN framework. Compared to metal nanoparticles, SACs preferentially facilitate end-on adsorption of O_2, which suppresses O-O bond cleavage and favors the $2\,e^-$ ORR pathway toward H_2O_2 production [11].

The incorporation of metal dopants into PCN strongly depends on the nature of the metal species.

Dopants may substitute carbon or nitrogen atoms within the lattice, occupy in-plane cavities, or reside in interlayer regions, each configuration influencing charge transport and surface reactivity differently. However, a major challenge associated with many metal dopants is the promotion of charge carrier recombination [17]. Metals with partially filled d-orbitals can introduce mid-gap states that act as recombination centers by facilitating electron falling back to their valence band [11].

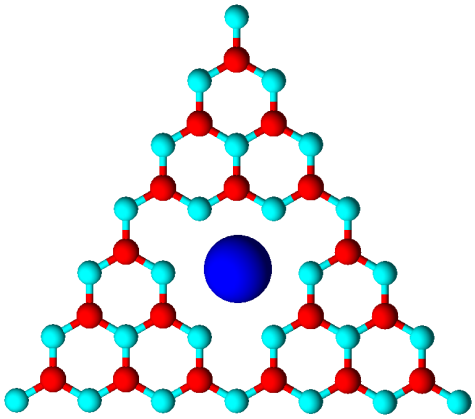

Figure 2.3: Potassium doped PCN

To mitigate this issue, this study focuses on metal dopants with a fully filled d10-orbital electronic configuration. Such metals have been reported to suppress recombination while enhancing visible-light absorption through band gap narrowing and improving redox capability via modulation of the valence and conduction band positions. These characteristics make d^{10}-orbital metals promising candidates for improving the photocatalytic efficiency of PCN [1].

2.3.5 Role of Potassium and Antimony Doping

Alkali-metal doping, particularly with potassium, has emerged as an effective strategy to enhance the photocatalytic performance of PCN. Potassium ions are predominantly located in the interlayer regions between polymeric melon chains, where they act as electrostatic binders that reduce interlayer distance and promote structural ordering [18]. The presence of interlayer K^+ ions induces internal electric fields that facilitate directional charge separation and transport, thereby suppressing electron-hole recombination and increasing the availability of photogenerated electrons for surface reduction reactions.

Some p-block metal and metalloids such as gallium and antimony could also become an attractive dopant as it have shown, when incorporated into the PCN framework, Sb species can modulate the local electronic structure without introducing deep trap states, which can transition-metal dopants may indtroduce [1] [11].

In addition to post-transition metals and alkali metals such as sodium (Na) and potassium (K) have attracted increasing attention as dopants for carbon nitride photocatalysts. These elements have been shown to enhance charge separation, distribution, and transfer of charge carriers. Potassium ions are doped between the melon chains as a binder and enhance charge separation and charge transport by forming charge transport channels. In contrast, Na ions are incorporated within the in-plane structure.

Notably, potassium-doped PCN have shown higher photocatalytic activity than its Na, and due to these reason will also be investigated in this study [18].

Although, single-element dopants have shown to improve acitivty of photocatalysts, then the benefit of new charge transport channels and d^{10} orbital electronic configuration is a unique characteristic of each element. Therefore, in order to enhance the photocatalytic activity of PCN further co-doping will also be investigated in this study can be used to take advantage of each elements characteristic and improve the photocatalyst.

3 Experimental

This chapter describes the synthesis procedures used to prepare the photocatalyst samples, as well as the characterization techniques employed to analyze their structural, optical, and electronic properties.

3.1 Synthesis of K-PCN

Potassium-doped PCN (K–PCN) was synthesized by solid-state thermal polymerization. Depending on the desired K loading, either 0.25, 0.75, 1.25, or 2.50 mmol of KCl was thoroughly mixed with 1 g of melamine using a mortar and pestle for 30 min. The resulting powder was transferred to a tube furnace and calcined under a nitrogen atmosphere. The temperature was increased from 25 to 560 °C at a rate of 4 °C min^{-1}, followed by stable temperature at 560 °C for 4 h. The obtained product was ground again for 30 min to ensure uniform particle size and improved dispersion.

Pristine PCN was prepared using the same procedure but without the addition of KCl.

3.2 Synthesis of Sb-PCN

For Sb-modified samples, 0.25, 0.75, 1.25, 2.50, 3.75, or 5.00 mmol of $NaSbF_6$ was dissolved in ethanol, after which 1 g of melamine was added and dispersed. The suspension was ultrasonicated for 60 min to promote homogeneous mixing. The solvent was then removed using a rotary evaporator under vacuum. The resulting white solid was ground and subsequently calcined following the same temperature program as described above. After calcination, the powder was again grounded for 30 min.

3.3 Synthesis of Sb-K-PCN

Co-doped Sb–K–PCN was synthesized following the same procedure as the 1.25 mmol Sb–PCN sample, with additional incorporation of KCl based on Sb:K molar ratios of 10:1, 10:3, and 10:5. These ratios correspond to 0.126 mmol, 0.376 mmol, and 0.622 mmol of KCl, respectively. The mixture was ground for 30 min and subsequently calcined using the same thermal treatment described above.

3.4 Characterization of materials

The following analytical techniques were used to characterize the structural, optical, and electronic properties of the synthesized photocatalysts.

3.5 XRD

Powder X-ray diffraction (XRD) was used to analyze the crystalline structure of the samples. XRD measurements were performed using a PANalytical X-ray powder diffractometer equipped with a Cu target X-ray source. Data were collected over a diffraction angle (2θ) range of 5 to 70° at a scanning rate of 16.7 $^\circ\,\mathrm{min}^{-1}$. The accelerating voltage and emission current were set to 40 kV and 45 mA, respectively. The obtained diffraction patterns were used to identify the crystalline phases and determine the crystal structures of the samples in 4.1

3.6 PL

Photoluminescence (PL) spectra were recorded using a Shimadzu RF-6000Plus fluorescence spectrophotometer. The samples were excited at a wavelength of 400 nm [1]. Emission spectra were collected over an appropriate wavelength range up 800 nm to capture the full photoluminescence response of the materials. All measurements were performed under identical instrumental settings to ensure comparability between samples.

3.7 XPS

X-ray photoelectron spectroscopy (XPS) was used to determine the oxidation states and chemical environments of the elements present in the samples. Measurements were performed using a Thermo Scientific K-Alpha X-ray photoelectron spectrometer. Spectra were acquired in fixed retarding ratio mode using Al Kα radiation ($h\nu = 1486.6$ eV), with an operating voltage of 12 kV and a pass energy of approximately 20 eV.

Energy calibration was performed by referencing the C 1s peak to a binding energy of 284.8 eV. The obtained spectra were analyzed to determine surface composition and chemical states as seen in 4.4.

3.8 UV-Vis DRS

Ultraviolet-Visible Diffuse Reflectance Spectroscopy (UV-Vis DRS) measurements were performed using a Shimadzu UV-3600Plus spectrophotometer. Spectroscopic-grade $BaSO_4$ was used as the reflectance standard for baseline calibration. Spectra were collected over the ultraviolet and visible wavelength range of 200 nm to 800 nm under identical instrumental conditions for all samples. The obtained reflectance data were used to evaluate the optical absorption properties of the materials in 4.5.

3.9 Fourier-Transform Infrared Spectroscopy

Fourier-transform infrared spectroscopy (FTIR) was used to identify the types of chemical bonds present in the samples, as variations in bonding correspond to differences in molecular structure. FTIR measurements were carried out using a TENSOR II FTIR Routine Spectrometer (Bruker Optics). The

instrument was operated in transmittance mode over a wavenumber range of 400-4000 cm^{-1}. A continuous gas flow of 400 $\frac{\mathrm{Nl}}{\mathrm{h}}$ was applied to minimize interference from atmospheric humidity and CO_2. Both sample and background spectra were recorded with 128 scans each, resulting in a total measurement time of approximately 210 seconds per sample. All measurements were performed on powdered samples. Background (baseline) spectra were collected using air, as the samples were analyzed in their undiluted form. To prevent cross-contamination, the spectrometer was thoroughly cleaned with ethanol between measurements.

3.10 EIS

Photoelectrochemical tests were conducted using a CHI-660E electrochemical workstation in a three-electrode configuration, using a sample coated working electrode, Ag/AgCl as the reference electrode, and a platinum as the counter electrode. The electrolyte used was a 0.1 M Na_2SO_4 solution.

To prepare the working electrode, the surface was first polished using a 0.05 L alumina slurry, followed by ultrasonic cleaning twice in acetone (10 min each), once in methanol (10 min), and finally rinsed with deionized water. The catalyst ink was prepared by dispersing 4.2 mg of the sample, 2.0 mg of carbon black, 25 L of nafion, 750 L of isopropanol, and 250 L of water. The mixture was ultrasonicated for 1 h and subsequently mixed using a vortex mixer to ensure homogeneity. The ink was drop-cast onto a 4 mm working electrode in two layers, allowing the first layer to dry for 10 min before applying the second.

Electrochemical impedance spectroscopy (EIS) was performed over a frequency range of 100 kHz to 1 Hz, at potentials ranging from 1.2 V to 0.1 V with 0.1 V intervals.

3.11 Photocatalytic experiment

For photocatalytic H_2O_2 production, 20 mg of catalyst was added to a sealed, jacketed glass reactor containing 36 mL demineralized water and 4 mL ethanol (70%). The suspension was sonicated for 3 min and purged with pure O_2 for 30 min. Irradiation was provided by a 500 W xenon lamp equipped with a cutoff filter ($\lambda > 420$ nm), while the suspension was continuously stirred with a magnet at 200 rpm. Running water cooled the reactor to maintain a consistent temperature for all experiments, as illustrated in Figure 3.1. To ensure consistent irradiation across all experiments, the light intensity was monitored before and after each run using a solar cell connected to a voltmeter; the measured output voltage ranged from 151 to 153 mV, see Appendix 12a. The reaction duration was 4 hours.

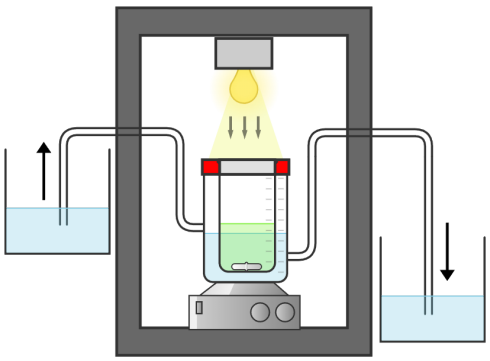

Figure 3.1: Schematic of photocatalytic experiment setup

At regular time intervals, 1–2 mL aliquots were withdrawn using a syringe, filtered using a Phenex PTFE 0.45 μm, and analyzed for H_2O_2 concentration using a colorimetric PACKTEST kit (WAK-H_2O_2, Kyoritsu Chemical-Check Laboratory Corp.). Measurements were performed using a PACKTEST digital spectrometer (ED723, GL Sciences Inc.).

The same procedure was followed for experiments at controlled pH values, with the only modification being adjustment of the solution pH using either HCl or NaOH prior to the sonication.

3.12 EPR

EPR experiments were performed only for Sb-K-PCN 10:3 sample using an ADANI SPINSCAN X-band spectrometer to monitor reactive species generated during photocatalysis. Both spin-trapping and spin-probing approaches were employed.

5,5-Dimethyl-1-pyrroline N-oxide (DMPO) was used as a spin-trapping agent for hydroxyl ($^{\bullet}$OH) and superoxide ($O_2^{\bullet-}$) radicals. Samples were prepared by dispersing 20 mg of catalyst in: (i) 0.5 mL of 0.044 M DMPO aqueous solution for $^{\bullet}$OH detection; (ii) 0.5 mL of 0.044 M DMPO in acetonitrile for $O_2^{\bullet-}$ detection.

2,2,6,6-Tetramethylpiperidine-1-oxyl (TEMPO) was used as a spin probe for photogenerated holes (h^+). Hole detection was carried out by monitoring the decrease of the TEMPO EPR signal under light irradiation.

Ex situ photoirradiation was performed using an LED light source with $\lambda \geq 420$ nm.

4 Results and discussion

In this chapter, the results of the experiments are presented and discussed. The aim is to systematically identify the optimal conditions and material compositions for enhanced photocatalytic performance. First, photocatalytic tests performed with varying KCl concentrations are analyzed to determine the concentration that yields the highest photocatalytic activity. Next, experiments using different metal dopants are evaluated, and the metal showing the most prominent photocatalytic acitivty is identified. This catalyst is subsequently tested at different loadings to determine the optimal composition. Following this, photocatalytic tests combining the optimal K loading with the selected metal-based catalyst are conducted to investigate potential synergistic effects. Finally, the samples are characterized using x-ray diffraction (XRD), photoluminescence (PL), time-resolved photoluminescence (TR-PL), X-ray photoelectron spectroscopy (XPS), Ultraviolet–Visible Spectrophotometry Diffuse Reflectance Spectroscopy (UV-Vis DRS), fourier transform infrared spectroscopy (FT-IR), electrochemical impedance spectroscopy (EIS) to relate their structural, optical, and electronic properties to the observed photocatalytic performance.

4.1 Structure of the photocatalyst

X-ray diffraction (XRD) was used to analyze the crystal structures of the synthesized samples.

All K-doped samples, as shown in Figure 4.1, exhibit the PCN diffraction peak at 27.39°, assigned to the interplanar stacking of aromatic units (002). A peak at 13.30°, observed for pristine PCN and K–PCN 0.25 mmol, corresponds to the in-plane tri-s-triazine units (100) [1]. At the highest K loading (2.50 mmol), an additional peak appears at 40.48°, which can be assigned to residual KCl (220) [19].

For pristine PCN, the (002) peak is relatively sharp and intense, indicating an ordered layered structure. Introducing a higher K loading leads to peak broadening and decreased intensity, suggesting reduced crystallinity and structural order. With further addition, the peak gradually weakens and becomes a broad hump for at K–PCN 1.25 mmol, indicating substantial lattice distortion and partial amorphization. The gradual disappearance of the (100) peak at 13°with increasing K loading further confirms distortion of the tri-s-triazine network. At the highest K loading (2.50 mmol), the peak at approximately 27.39°is completely gone, but a new peak has appeared at 28.23 °, corresponding to crystalline KCl (200) formation, supported by the appearance of the KCl (220) peak.

This evolution of crystallinity suggests that K initially disrupts the PCN lattice. However, in the study [18], it suggests that K promotes crystallinity and structural reorganizes to the PCN structure. Therefore, a possible reason for 4.1 for showing the opposite could be due to KCl still being present in the sample together with the incorporated K into the interplane, where residue KCl disrupts the structure. KCl still being present is also supported by the study [20], where there is an additional step of washing KCl out of the sample and drying it afterwards, which wasn't part of this study's method in synthesising K-doped

PCN, see Section 3.1.

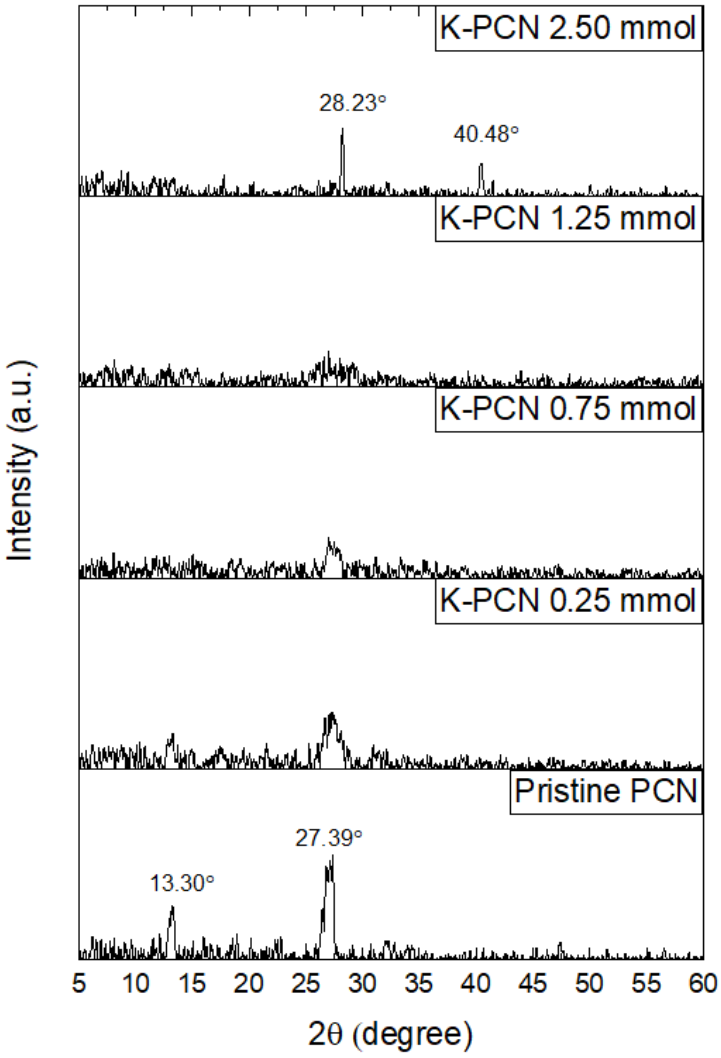

Figure 4.1: XRD of Pristine and K-doped PCN samples.

All Sb-doped samples, as shown in Figure 4.2, exhibit the characteristic PCN (002) peak at approximately 27.5°to 27.7°, indicating that Sb incorporation does not disrupt the main PCN framework. Additional peaks at approximately 32.13°, 46.13°, 54.63°, and 57.23°become more pronounced with increasing Sb concentration. These peaks correspond to Sb_2O_3 crystalline phases: (400), (440), (622), and (444), respectively. The presence of Sb_2O_3 likely arises from partial oxidation of Sb during high-temperature calcination [21].

The sharpening of the PCN (002) peak with increasing Sb suggests enhanced crystallinity. The consistent peak position implies that Sb atoms likely positioning in the planar pores, where it can bind with six nitrogen lone electron pairs, it forms a coordinated structure with surrounding N atoms, within the PCN structure rather than positioning itself between layers [1].

Enhanced photocatalytic activity is observed with increasing Sb loading up to 2.50 mmol, after which activity declines, likely due to overdoping, which causes excess Sb to faciliate recombination centers that reduces charge carriers [22]. The improved photocatalytic activity may be attributed to bandgap

narrowing by Sb incorporation, enabling wider light absorption, and improved light absorpbance, see Section 2.3.5.

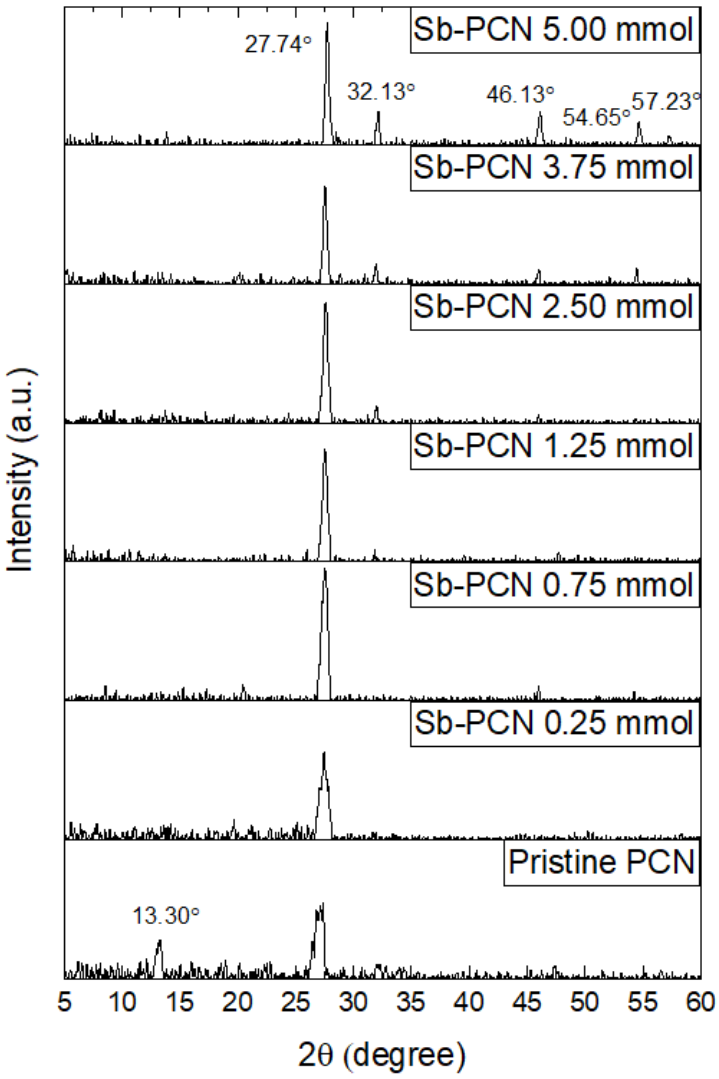

Figure 4.2: XRD of Pristine and Sb-doped PCN samples.

For the Sb–K co-doped samples, Figure 4.3, the (002) PCN peak at approximately 27.5°can be observed for all Sb-K-PCN samples. Only the Sb–K-PCN (10:1) sample exhibits additional peaks at 11.65°from tri-s-triazine (100), 32.08°from Sb_2O_3 (400), 45.82°from Sb_2O_3 (440), and 54.44°from Sb_2O_3 (622), indicating the presence of Sb2O3 in the sample.

The main (002) peak shows no significant shift across the Sb-K-PCN samples, suggesting that simultaneous incorporation of Sb and K does not substantially alter the PCN framework.

The reason crystallinity remains relatively stable in Sb–K-PCN samples, despite KCl showing to reduce crystallinity previously, could be related to the differences in charge density and bonding tendencies between Sb^{3+} and K^{+}. Sb^{3+} can bind in-plane with N atoms, forming stable coordination centers that anchor the structure. The nitrogen environment is strongly influenced by Sb^{3+}, which is supported by the study by Teng et al. [11], showing that Sb^{3+} fits best with 3.3 N atoms, suggesting that Sb coordinates with three neighboring N atoms.. These interactions counteract the lattice distorting effects observed

from residue KCl.

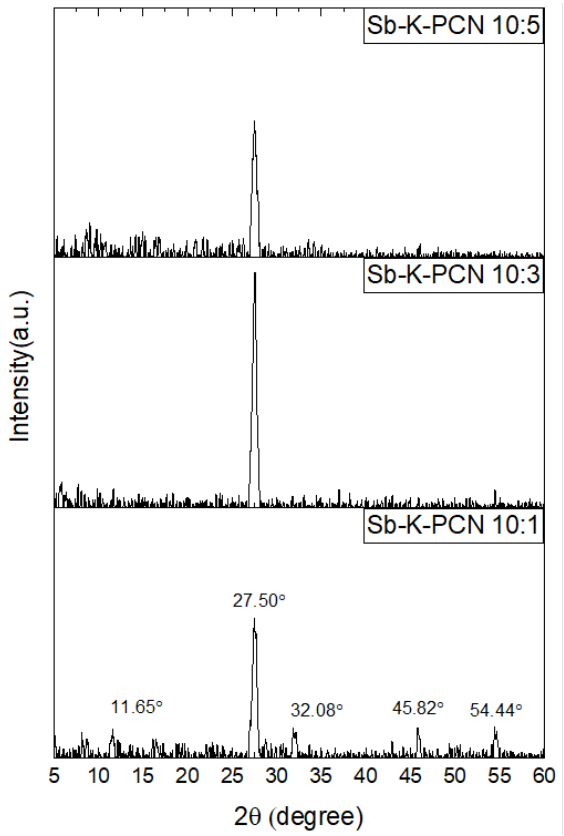

Figure 4.3: XRD of co-doped PCN samples.

4.2 Charge Carrier Dynamics of the photocatalyst

Steady-state PL emission spectroscopy was used to evaluate the recombination behavior of photogenerated charge carriers in the photocatalysts. PL emission in semiconductors arises from the radiative recombination of electrons and holes. Therefore, a lower PL intensity generally suggests suppressed radiative recombination, which is associated with more efficient charge separation and enhanced charge transport to the surface, where redox reactions occur.

As shown in Figure 4.4, all PCN samples exhibit a broad visible emission band. Pristine PCN displays a strong emission peak at approximately 483 nm, while K-doped PCN emits near 472 nm, Sb-PCN near 510 nm, and Sb–K-PCN around 486 nm. Doping with either K or Sb reduces the PL intensity, although to different extents. K-doped PCN shows only a modest reduction, whereas Sb-doped PCN exhibits a strong decrease. The Sb–K co-doped sample shows a PL suppression similar to that of Sb-PCN.

The modest decrease in PL of K-PCN suggests thatKintroduce some mid-gap states capable of trapping or redirecting charge carriers into non-radiative pathways or lower-energy radiative pathway, which also explains the broadining of the emission that overlaps Pristine PCN's emission tail. The strong PL decrease in Sb-doped samples indicates that Sb introduces even more electronic states within the bandgap. These Sb-related mid-gap states can temporarily trap electrons, promoting non-radiative charge transfer to surface catalytic sites rather than radiative recombination. This enhances charge separation

and increases the probability that photogenerated electrons participate in surface redox reactions such as the oxygen reduction reaction (ORR).

Consistent with this behavior, the doped PCNs exhibit shorter TR-PL lifetimes than pristine PCN, indicating the introduction of fast non-radiative decay pathways. These pathways are attributed to efficient charge transfer to dopant-induced trap states and surface reaction sites, rather than radiative electron–hole recombination.

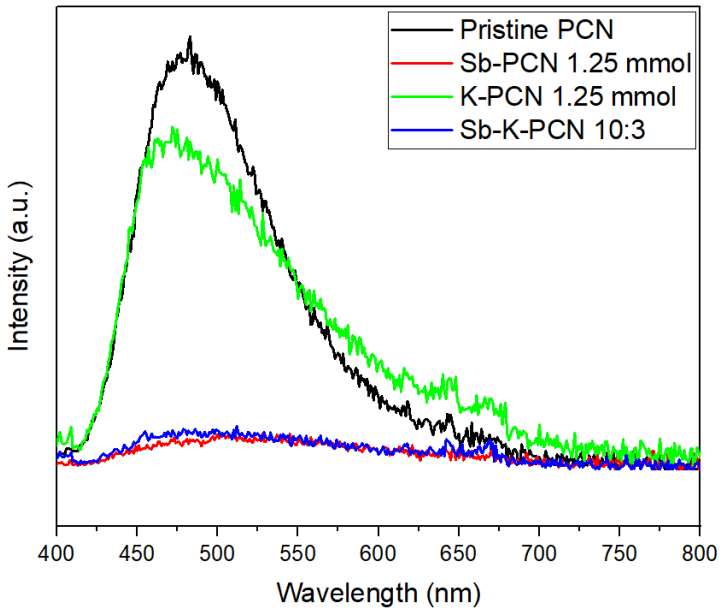

Figure 4.4: PL spectra of the Pristine PCN, Sb-PCN 1.25 mmol, K-PCN 1.25 mmol, and Sb-K-PCN 10:3 samples.

4.3 Charge-Carrier lifetimes of Photocatalyst

TR-PL was used to further investigate the charge-carrier lifetimes of the photocatalysts. The photoluminescence decay curve can then be fitted by the Equation (4.1) and is shown in Figure 4.5.

$$\mathrm{I(t)}=\mathrm{B}_1 \cdot \exp(-\mathrm{t}/\tau_1) + \mathrm{B}_2 \cdot \exp(-\mathrm{t}/\tau_2) + \ + \mathrm{B}_3 \cdot \exp(-\mathrm{t}/\tau_3) \tag{4.1}$$

Where I(t) is intensity in relation to time, B_1, B_2, and B_3 are the pre-exponential factors, and τ_1, τ_2, and τ_3 are the corresponding lifetimes.

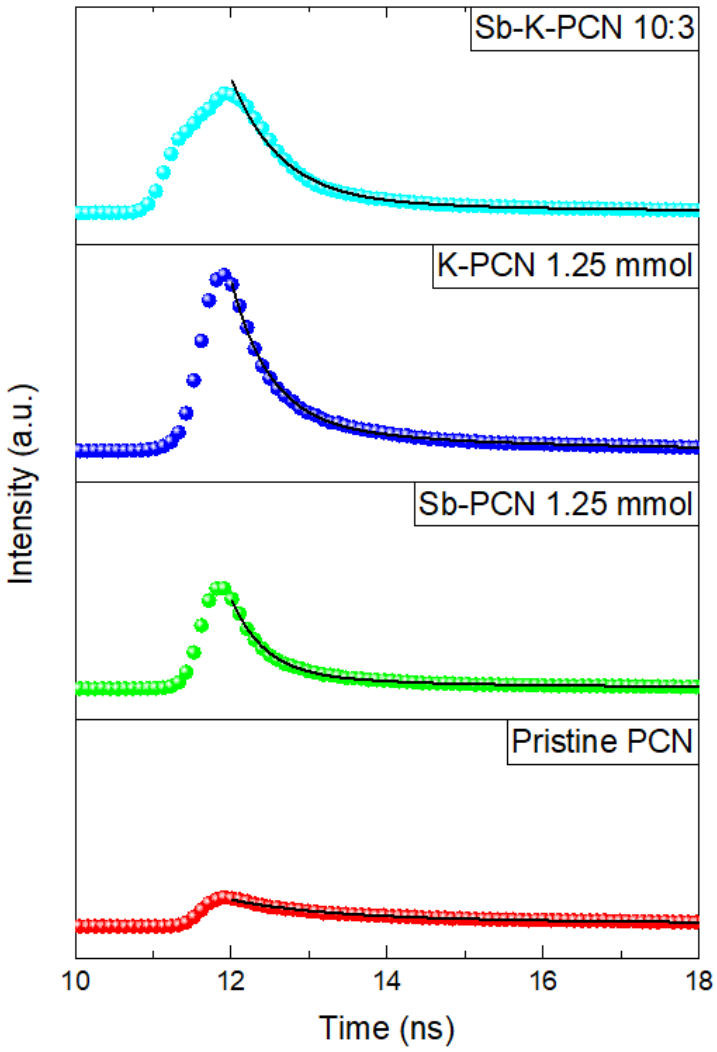

Figure 4.5: TR-PL spectra of the photocatalysts.

The average fluorescent lifetime τ_a can be calculated from the following Equation (4.2).

$$\tau_{\text{avg}} = \frac{B_1\,\tau_1^2 + B_2\,\tau_2^2 + B_3\,\tau_3^2}{B_1\,\tau_1 + B_2\,\tau_2 + B_3\,\tau_3} \tag{4.2}$$

This corresponds to the fitted lifetimes that are summarized in Table 4.1. All doped samples exhibit significantly shorter average lifetimes compared to Pristine PCN, indicating faster charge-carrier decay. Combined with the reduced PL intensity, this suggests that non-radiative recombination dominates, facilitating more efficient charge transfer to the redox-active sites.

Sample	τ_1 (ns)	B_1 ($\times 10^3$)	τ_2 (ns)	B_2 ($\times 10^3$)	τ_3 (ns)	B_3 ($\times 10^3$)	χ^2	τ_{avg} (ns)
Pristine PCN	1.20	3.02	6.51	1.30	32.97	0.19	1.16	14.35
Sb-PCN 1.25 mmol	0.43	14.86	2.69	2.14	18.68	0.09	1.31	3.65
K-PCN 1.25 mmol	0.49	26.87	2.57	4.65	17.40	0.18	1.57	3.23
Sb-K-PCN 10:3	0.63	22.27	3.57	2.08	21.17	0.12	1.87	3.66

Table 4.1: The pre-exponential factors (B_1, B_2, and B_3), lifetimes (τ_1, τ_2, and τ_3), and average lifetimes (τ_{avg}).

4.4 Elemental Composition and Dopant Interactions in the photocatalyst

X-ray photoelectron spectroscopy (XPS) was used to obtain full survey spectra, shown in Figure 4.6, as well as high-resolution spectra for the C 1s, F 1s, K 2p, N 1s, Na 1s, and O 1s. These spectra provide insight into the elemental composition of the samples and the influence of dopants on the chemical interactions between the constituent elements.

All observed peaks are in good agreement with reported reference binding energies from the literature. Minor deviations of up to ± 0.3 eV from reference values are expected and have been taken into account [23]. After peak fitting and convergence using the OriginPro Peak Analyzer, all peaks fell within the expected reference ranges, with the exception of the N–C_3 component in the Sb–K–PCN 10:3 sample and the H_2O-related peaks in the K–PCN (1.25 mmol) and Sb–K–PCN 10:3 samples.

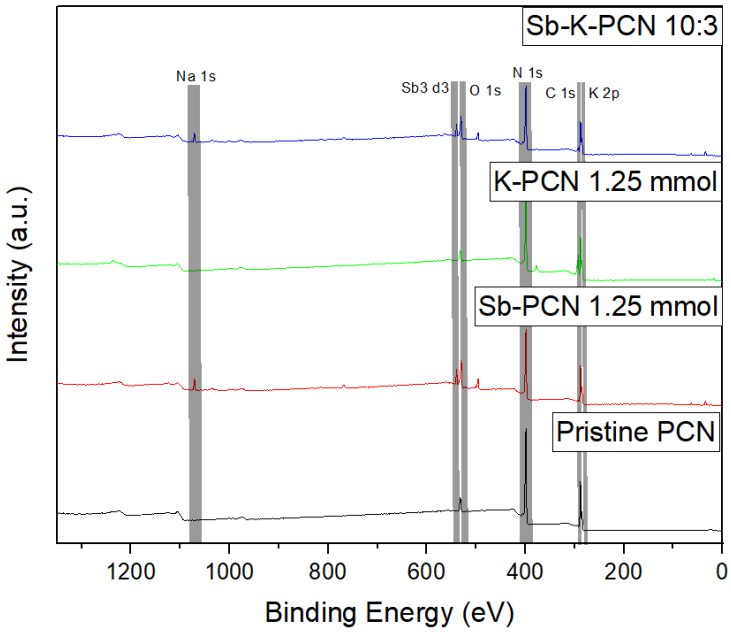

Figure 4.6: Full XPS Survey of the element peaks found for the photocatalyst samples.

For the peaks located in the C 1s orbital spectrum all samples showed peaks at approximately 284.9 eV, 286.3 eV and 288.3 eV, which are in accordance with the binding energies of C-C, $C \equiv N$, and N-C=N that can be attributed to adventitous carbon and sp2 hybridized carbon in the heptazine rings [11].

Moreover, new peaks at around 292.8 eV and 295.5 eV can be observed for K-PCN and Sb-K-PCN, which are in accordance with the binding energies ofK2p3/2 andK2p1/2 [24]. Together with the small

shift of the N 1s peak to lower binding, this indicates that K was incorporation into PCN. This is also supported by the decrease of the relative intensity of the peak corresponding to N-C=N bond at 288.3 eV in comparison to Pristine PCN, which could indicate that nitrogen partly breaks some of the C=N bonds to form new bonds with K instead.

The same can be said for Sb-doped samples, where there is a decrease in N-C=N bond at 288.1 eV in comparison to Pristine PCN, together with an increased intensity of Sb-N bonds observed at around 530.2 eV and 539.5 eV compared.

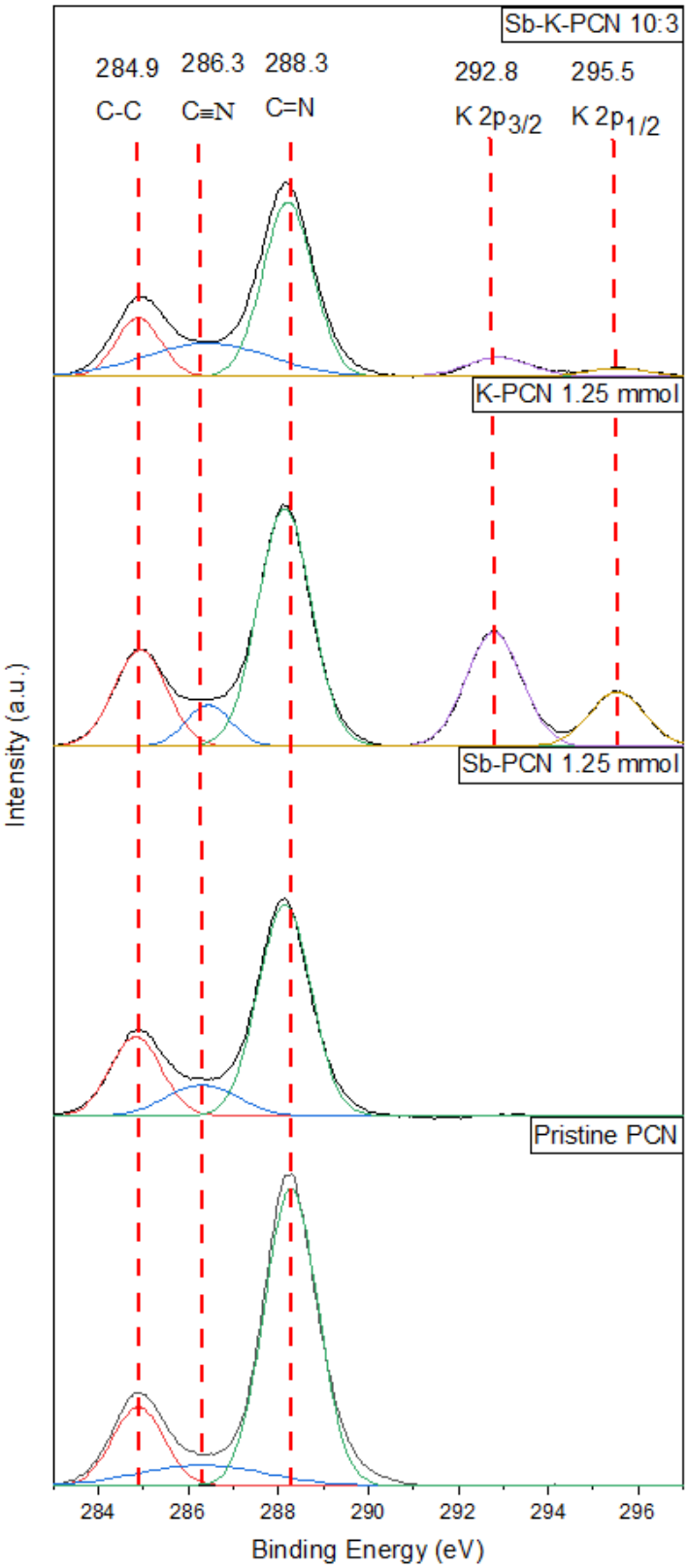

Figure 4.7: C1s spectra of XPS

For the K 2s spectra there can be observed one peak at approximately 377.5 for K 2s for K-PCN and Sb-K-PCN, which again supports that K is present.

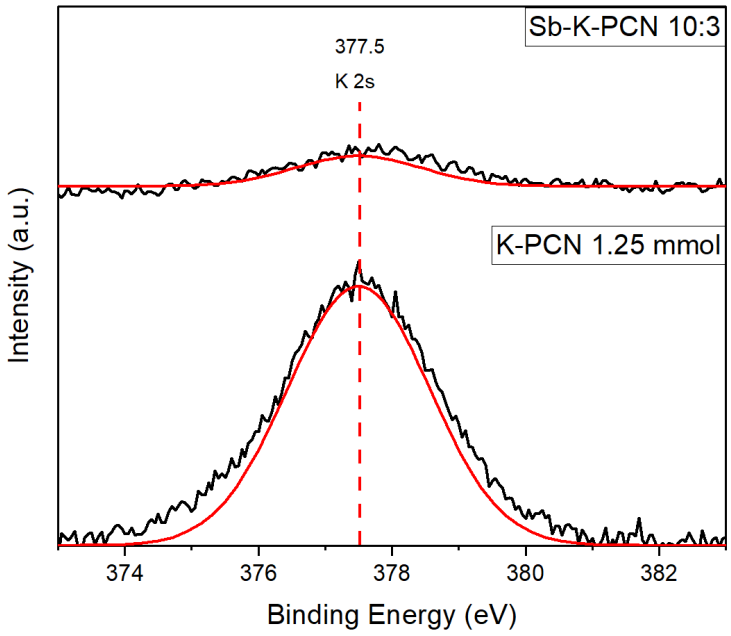

Figure 4.8: K 2s spectra of XPS

The N 1s spectra can be deconvoluted into four peaks located at approximately 398.4, 398.7, 400.1, and 401.1 eV, which can be assigned to Sb-N bonding, sp^2-hybridized nitrogen in C=N-C groups within the heptazine units of PCN, tertiary nitrogen (N-$(C)_3$), and the amino groups, such as C-NH_x species [11]. As expected, the Sb-N peak is observed only in the Sb-PCN and Sb-K-PCN samples, confirming the successful incorporation of Sb into the PCN framework.

Upon doping with Sb and K with the exception of the co-doped, there can observed a slight shift of N 1s peak position from Pristine PCN's peak position at 398.75 towards a lower binding energy for the N 1s, suggesting an increase in electron density around nitrogen due to charge transfer from the dopants to the PCN framework. The shift could be due to altered local bonding environment resulting from the Sb-N and K-N interaction causing a shift to 398.65 for Sb-doped and 398.60 eV for K-doped, whereas Sb is incorporated into the in-planar PCN framework, while K binds through inter-layer interaction, thus explaining why the chemical environment shift more with K.

For the co-doped Sb-K-PCN 10:3 samples, then N 1s peak position remains the same, which suggest low or no interaction with nitrogen.

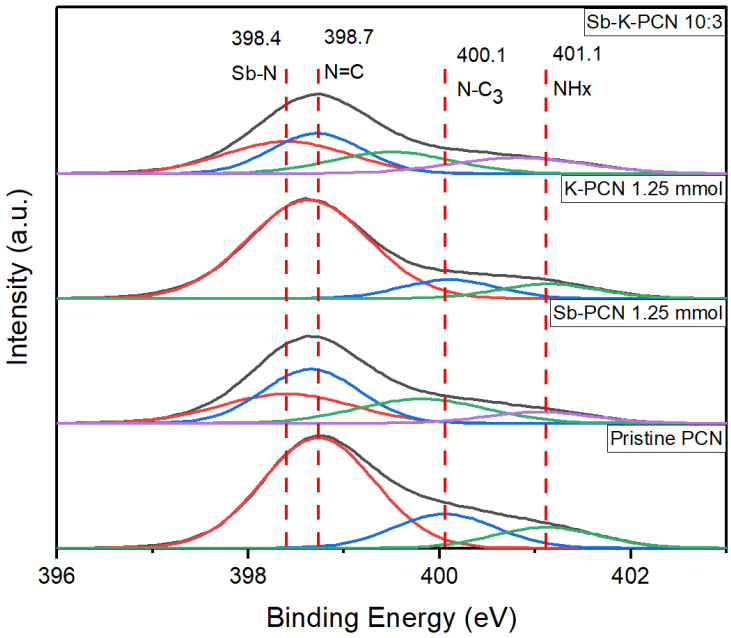

Figure 4.9: N 1s spectra of XPS

In the O 1s spectra, an overlap with the Sb 3d spectra is observed for the Sb-doped samples. Four peaks can be identified at approximately 530.2, 531.6, 532.5, and 539.5 eV, corresponding to Sb $3d_{5/2}$, C=O species, surface-adsorbed H_2O, and Sb $3d_{3/2}$, respectively. The Sb 3d peaks are observed only in the Sb-doped samples. Their binding energies are close to those reported for Sb_2O_3 (Sb $3d_{5/2}$ at 530.5 eV and Sb $3d_{3/2}$ at 539.8 eV), indicating that Sb predominantly exists in the +3 oxidation state in the doped PCN. Due to the overlap between Sb $3d_{5/2}$ and the O 1s signal, the O 1s peak is broadened and slightly shifted toward lower binding energy [11]. The K-doped sample also broadens slightly towards lower bidning energy and increases its peak position from 531.70 eV to 531.95 eV. In the case of the K-doped samples, this could explained by K interaction with oxygen through electrostatic interactions, thus decreasing oxygens electron density, and casuing O 1s electrons to be held more tightly and increase binding energy.

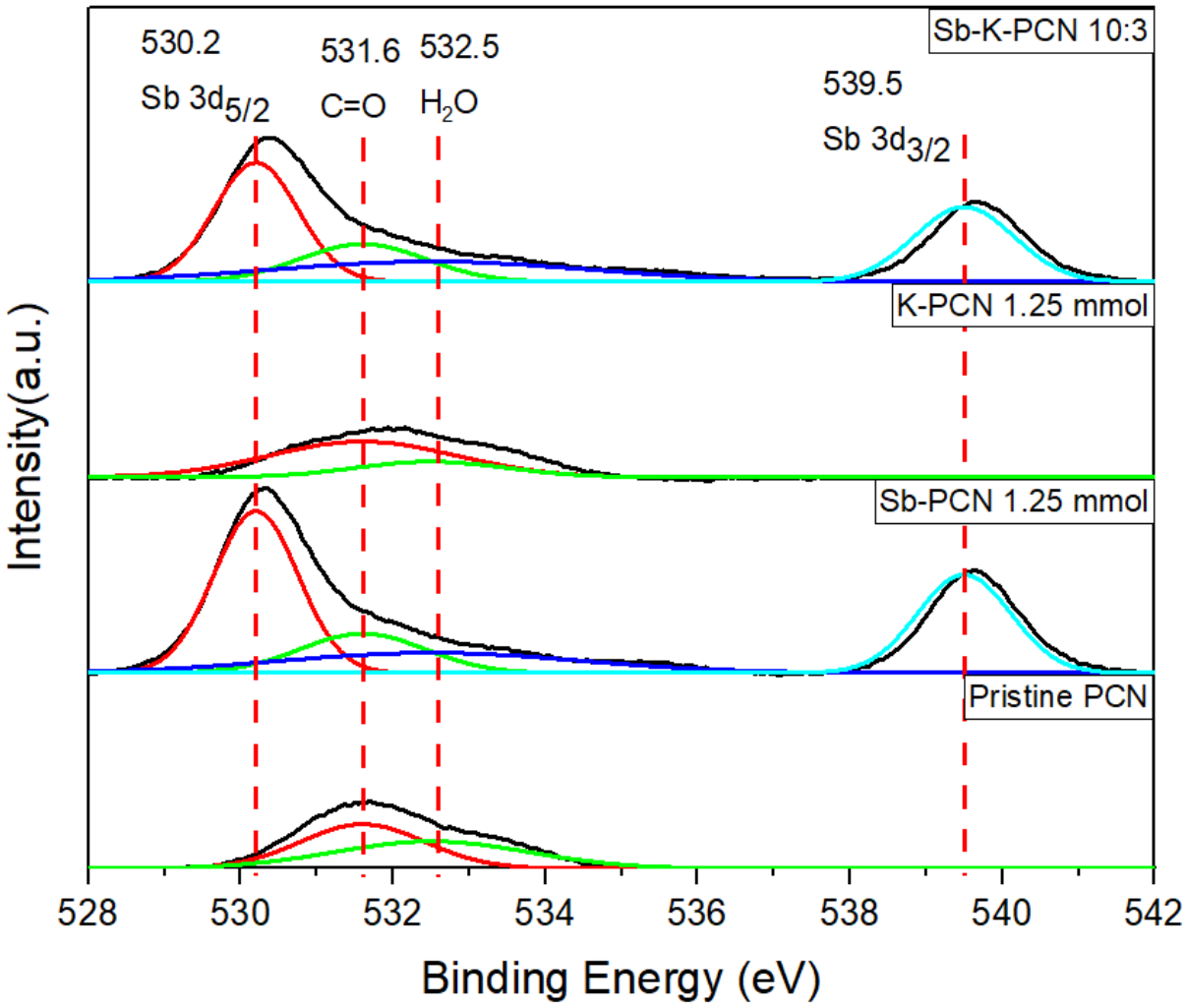

Figure 4.10: O 1s and Sb 3d spectra of XPS

Lastly, there were no peaks found for the F1s spectra. However, there was observed one in the Na 1s spectra in Figure 4.11. A single Na 1s component appears at approximately 1071.3 eV, and its position and intensity remain essentially unchanged between the Sb-PCN (1.25 mmol) and Sb-K-PCN (10:3) samples. Like the study [11], then Na remains from the precursor. As discussed in 2.3.5, then Na can have a enhancing photocatalytic effect, thus the presence of it cant exclude its impact on the photocatalytic effect in this study.

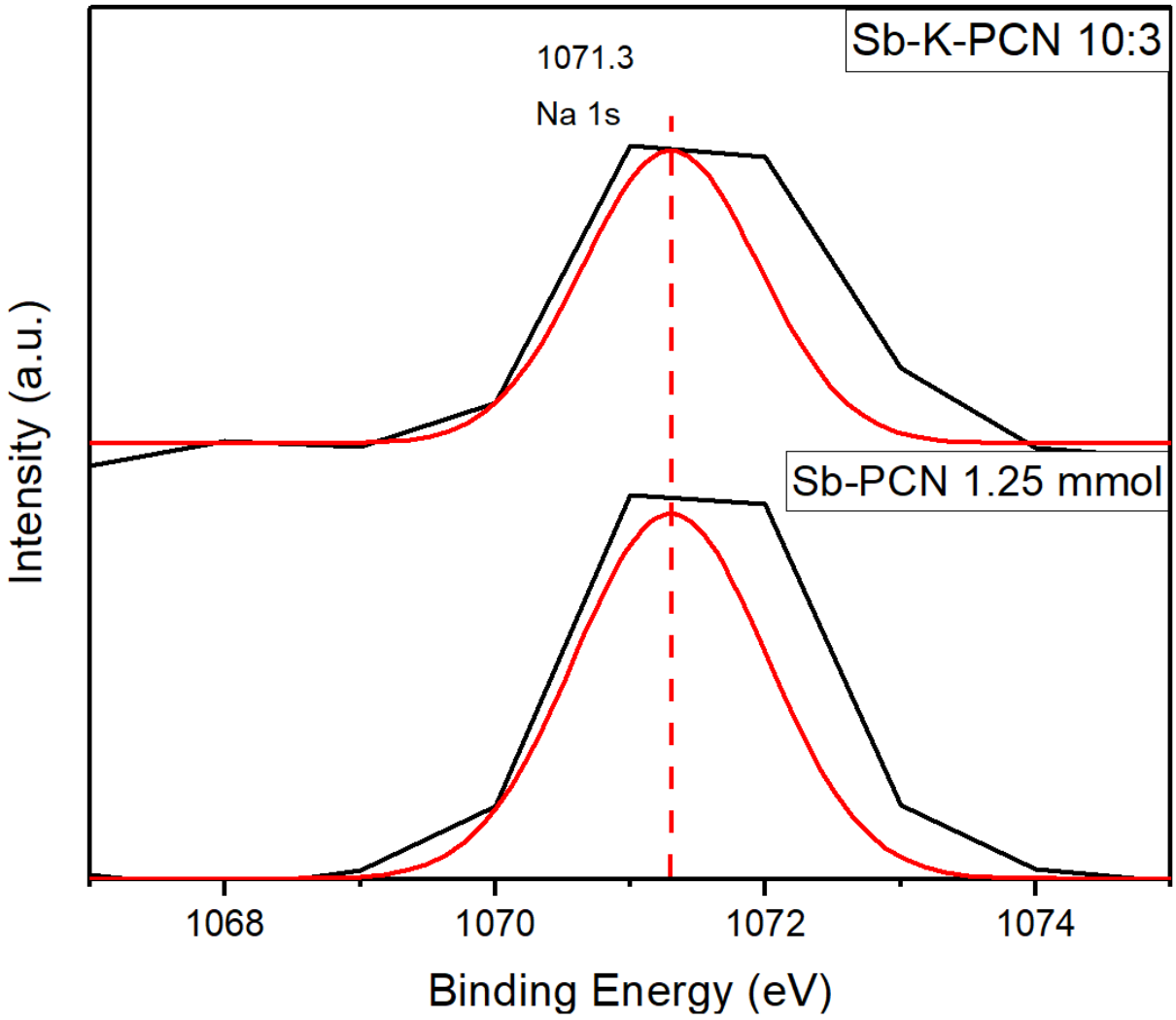

Figure 4.11: Zoom of the spectra of the XPS corresponding to the Na 1s binding energy.

4.5 Optical Absorption and Bandgaps in photocatalyst

The UV-Vis DRS was used to investigate the optical absorption properties of the samples and to estimate their bandgap energies. This analysis provides insight into the influence of Sb and K incorporation on the electronic structure of PCN and its potential impact on charge-carrier excitation behavior. The UV–Vis absorption spectra of all samples are presented in Figure 4.12, while the corresponding absorption edge values are summarized in Table 4.2. All samples exhibit strong absorption in the UV region, followed by a sharp decrease near their absorption edges.

The pristine PCN shows strong absorption in the UV-A region (320–400 nm), which is characteristic of π–π^* transitions in the conjugated heptazine framework. Upon doping, a clear redshift of the absorption edge is observed, seen in Table 4.2, indicating an extension of light absorption toward longer wavelengths with lower photon energy. This redshift suggests a reduction in the bandgap, which can be attributed to the introduction of new electronic states and enhanced delocalization of π-electrons within the PCN framework. As a result, all doped samples exhibit increased absorption in the visible-light region (380–750 nm) compared to pristine PCN.

Sample	Absorption Edge (nm)
Pristine PCN	472.32
Sb-PCN 0.25 mmol	498.61
Sb-PCN 0.75 mmol	503.81
Sb-PCN 1.25 mmol	502.99
Sb-PCN 2.50 mmol	551.17
K-PCN 1.25 mmol	486.92
Sb-K-PCN 10:1	526.39
Sb-K-PCN 10:3	509.61
Sb-K-PCN 10:5	503.22

Table 4.2: Absorption edge values from UV-Vis DRS measurements.

The absorption intensity is strongly wavelength-dependent. In the UV region (100–400 nm), the Sb-PCN 0.25 mmol sample exhibits the highest absorption intensity, whereas in the visible-light region (400–700 nm), Sb-PCN 2.50 mmol shows the strongest absorption. The enhanced visible-light absorption at higher Sb concentrations can be attributed to more pronounced bandgap narrowing, which allows excitation of electrons using lower-energy photons. Consequently, Sb-PCN 2.50 mmol absorbs visible light most efficiently due to its narrowest bandgap. In contrast, the superior UV absorption of Sb-PCN 0.25 mmol suggests that low Sb doping minimally disturbs the π-conjugated network, preserving strong high-energy electronic transitions.

Since UV light constitutes only a small fraction of the solar spectrum, enhanced absorption in the visible-light region is particularly important for photocatalytic activity. Therefore, the strong visible-light absorption is expected to be more beneficial for photocatalytic performance than enhanced UV absorption alone.

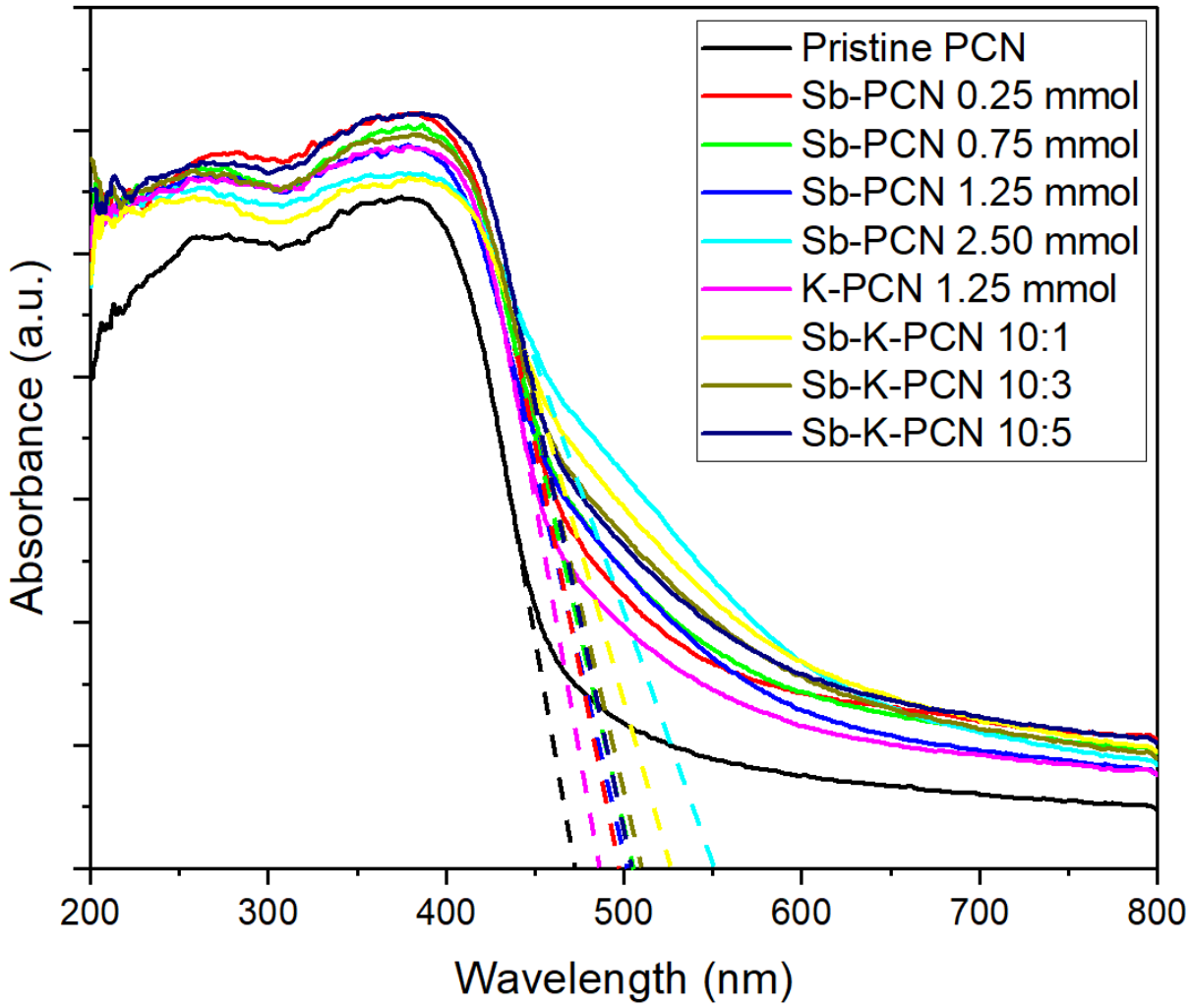

Figure 4.12: UV-Vis DRS spectra of photocatalysts

The optical bandgap energies of the samples were estimated using Tauc plots derived from UV–Vis diffuse reflectance spectroscopy (DRS) data. Since diffuse reflectance measurements do not directly provide absorption coefficients, the reflectance spectra were converted using the Kubelka–Munk function, which relates reflectance to absorption in optically thick powdered samples. The transformed absorption data were analyzed using the Tauc relation, see Equation 4.3.

$$(\alpha h\nu)^{1/n} = B(h\nu - E_g) \tag{4.3}$$

where α is the absorption coefficient, h is Planck's constant (6.62×10^{-34} J·s), ν is the photon frequency, E_g is the optical bandgap energy, and n depends on the nature of the electronic transition. As PCN synthesizied with melamine is primarily an indirect band gap semiconductor, as seen in 2.3.3; therefore, $n = 2$ was used in this study.

The absorption coefficient was calculated using:

$$\alpha = \frac{2.303A}{d} \tag{4.4}$$

where A is the absorbance, d is the optical path length, and 2.303 is the conversion factor from $\log_{10}$ to the natural logarithm. The photon energy ($h\nu$) was calculated using:

$$h\nu = \frac{1240}{\lambda} \quad \text{(eV)} \tag{4.5}$$

where λ is the wavelength in nanometers. Tauc plots were constructed by plotting $(\alpha h\nu)^{1/2}$ as a function of photon energy ($h\nu$). The indirect bandgap energy of each sample was determined by extrapolating the linear region of the steepest slope to the energy axis, as shown in Figure 4.13. The calculated bandgap values are summarized in Table 4.3.

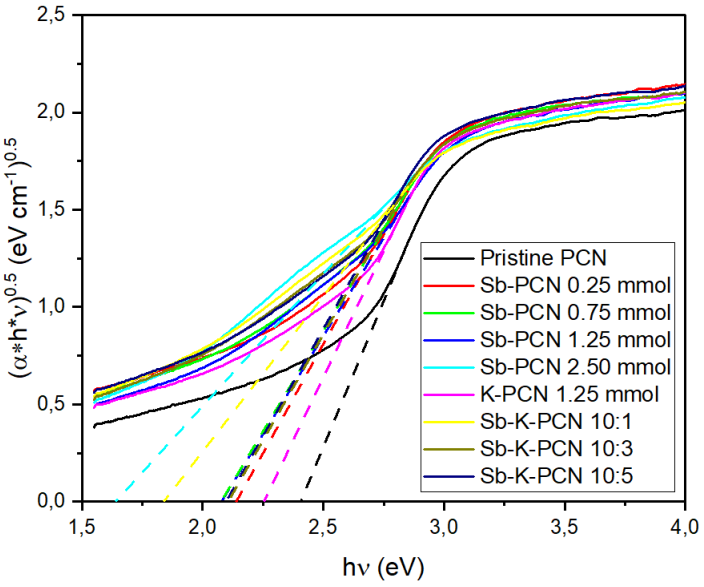

Figure 4.13: Bandgap from UV-Vis DRS spectra

Table 4.3: Indirect bandgap energies for the samples.

Sample	**Indirect (eV)**
Pristine PCN	2.40
Sb-PCN 0.25 mmol	2.14
Sb-PCN 0.75 mmol	2.08
Sb-PCN 1.25 mmol	2.08
Sb-PCN 2.50 mmol	1.64
K–PCN 1.25 mmol	2.25
K–Sb-PCN 10%	1.84
K–Sb-PCN 30%	2.01
K–Sb-PCN 50%	2.09

All doped samples exhibit reduced bandgap energies compared to pristine PCN, which possesses the largest direct and indirect bandgaps. The bandgap reduction in K-doped PCN is attributed to enhanced π-electron delocalization and the formation of mid-gap states near the conduction band, although K^+ is less effective in generating mid-gap states. Consequently, K-PCN retains a relatively wider bandgap

compared to Sb-doped samples.

In contrast, Sb-doped PCN exhibits a more pronounced bandgap narrowing, particularly at higher Sb concentrations. This effect is attributed to the hybridization of Sb 5p orbitals with PCN orbitals, leading to the formation of mid-gap states and modification of the valence band structure. Additionally, Sb^{3+} may attract electron density from neighboring nitrogen atoms, further elevating the valence band. These effects altogether explains why Sb-PCN 2.50 mmol achieves the narrowest bandgap among all samples.

Interestingly, co-doping with Sb and K results in a synergistic bandgap narrowing at low K content, Sb-K-PCN 10:1, where both dopants contribute simultaneously to electronic structure modification. However, at higher K loads for Sb-K-PCN 10:3 and 10:5, the bandgap slightly increases, suggesting that excessive K incorporation may disrupt the optimal electronic interaction between the dopants and the PCN framework.

4.6 Chemical Structure of photocatalyst

The chemical structure of the samples was analyzed using FT-IR spectroscopy. All samples exhibit very similar characteristic absorption features, with the main differences being the appearance of an additional peak at 993 cm^{-1} for the K-doped samples and the absence or significant weakening of the peak at around 1150 cm^{-1} for the Sb-K-PCN samples.

A broad absorption band observed between 2800 and 3600 cm^{-1} is assigned to N–H and O–H stretching vibrations associated with surface amino groups and adsorbed hydroxyl species [25]. An additional absorption band located at approximately 2170 cm^{-1} can be attributed to the stretching vibration of cyano groups (–C≡N), which is also supported by the presence of C≡N species identified in the C 1s XPS spectra [26].

This observation is consistent with previous studies [26], which report that the formation of C≡N groups can be induced by the incorporation of alkali metal ions such as K or Na into graphitic carbon nitride. These alkali metal ions are suggested to play a significant role in promoting cyano group formation. Furthermore, the presence of C≡N groups has been reported to enhance charge separation and thereby improve photocatalytic activity [27, 26].

Strong absorption bands in the range of approximately 1230 to 1630 cm^{-1} are attributed to the stretching vibrations of aromatic C–N and C=N bonds within the heptazine framework [25]. These bands originate from stretching modes of trigonal units connected by C–N(–C)–C and C–NH–C moieties, confirming the preservation of an extended conjugated C–N network after incorporation of the dopants [25]. Additional peaks observed at approximately 993 cm^{-1} and 1153 cm^{-1} can be assigned to the symmetric and asymmetric vibrations of N–C_2 bonds associated with K–N–C_2 species. For the Sb-K co-doped samples, the peak at 1153 cm^{-1} is significantly weakened, while the peak at 993 cm^{-1} is absent, indicating a reduced contribution of K-related vibrational modes [26].

The last peak is located at approximately 806 cm^{-1} corresponds to the bending mode of tri-s-triazine (heptazine) units, which is a characteristic fingerprint of PCN and further confirms the preservation of the heptazine framework [25].

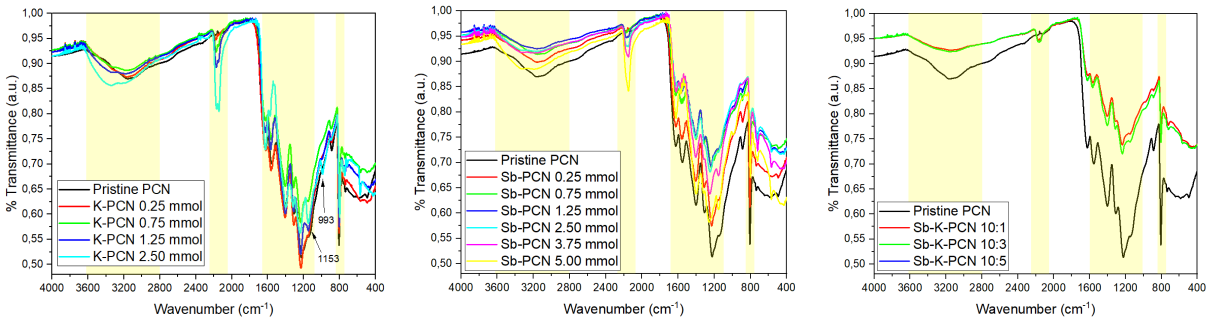

(a) **(b)** **(c)**

Figure 4.14: FT-IR spectra of samples: (a) K-PCN, (b) Sb-PCN, and (c) Sb-K-PCN.

4.7 Charge-Transfer and Carrier Mobility in photocatalyst

Electrochemical impedance spectroscopy (EIS) was used to evaluate the charge-carrier migration efficiency and interfacial charge-transfer behavior of the prepared samples.

As shown in Figure 4.15 and summarized in Table 4.4, Pristine PCN exhibits a significantly lower charge-transfer resistance (R_{ct}) of 604 Ω, represented by the diameter of the semicircle, compared to the bare electrode 1843 Ω. This confirms that the π-conjugated $tri - s - triazine$ framework of PCN facilitates efficient electron transport.

Both Sb- and K-doped PCN samples show further reductions in R_{ct} relative to pristine PCN. Among the K-doped samples, K-PCN 1.25 mmol exhibits the lowest charge-transfer resistance of 315 Ω. This behavior is consistent with the role of K^+ as an electron donor, which introduces charge-transport channels and enhances charge-carrier mobility within the PCN framework.

For the co-doped samples, Sb-K-PCN 10:1 shows the lowest resistance of 334Ω, indicating a synergistic effect between Sb and K dopants. However, increasing the K content leads to a gradual increase in R_{ct}, with Sb-K-PCN 10:3 and Sb-K-PCN 10:5 exhibiting resistances of 523 Ω and 908 Ω, respectively. This trend suggests that while a small amount of K^+ can compensate for the higher resistance of Sb-PCN 1.25 mmol and enhance interfacial charge transfer, excessive K doping becomes counteractive. The increased resistance at higher K loadings may be attributed to disruption in the optimal electronic interaction between the dopants and the PCN framework similar to the significant lower bandgap showed for the 3.8.

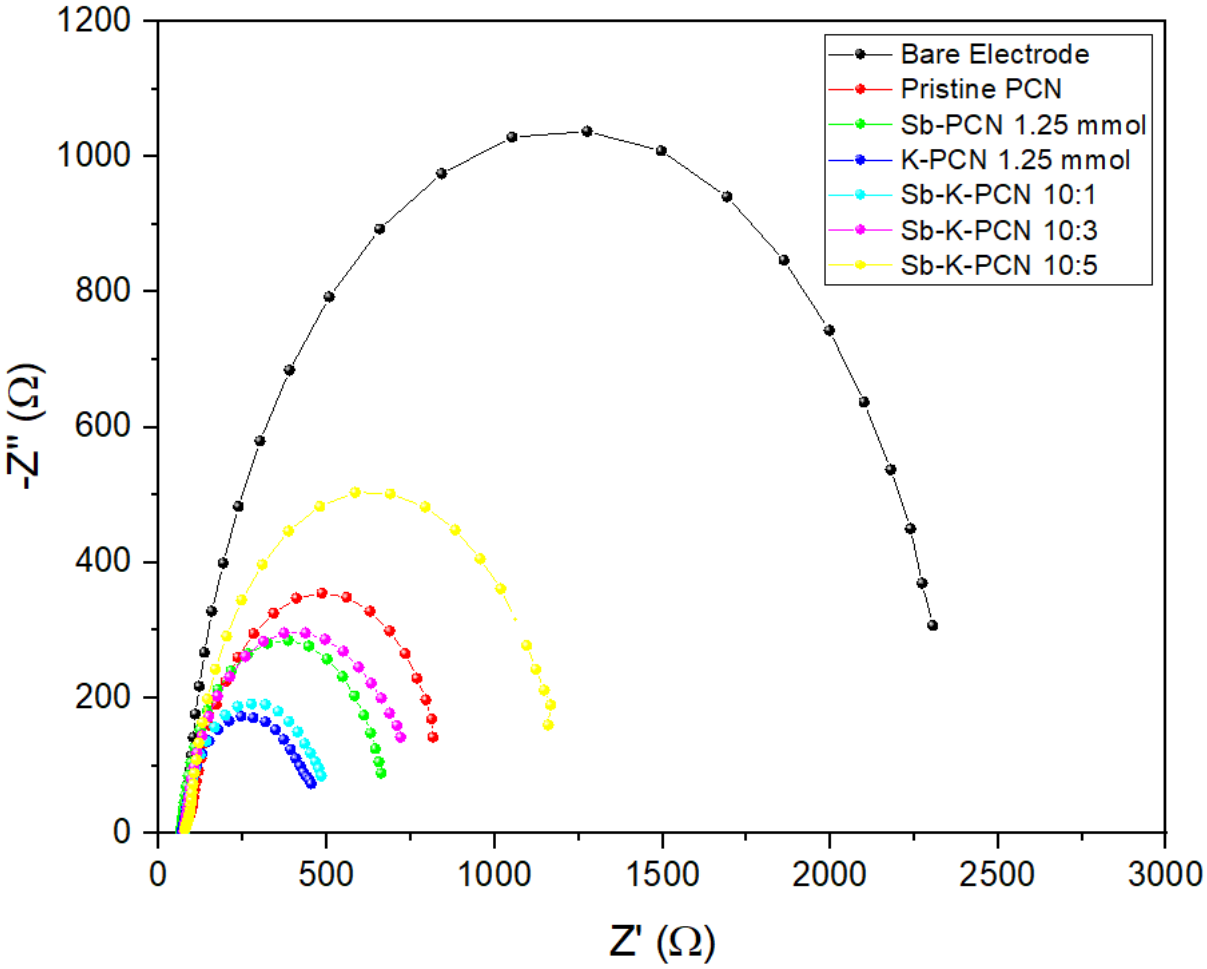

Figure 4.15: Nyquist plot of obtained EIS measurements for Pristine PCN, K-PCN, Sb-PCN, and Sb-K-PCN samples.

Sample	Charge-transfer resistance (Ω)
Bare electrode	1843
Pristine PCN	604
Sb-PCN 1.25 mmol	498
K-PCN 1.25 mmol	315
Sb-K-PCN 10:1	334
Sb-K-PCN 10:3	523
Sb-K-PCN 10:5	908

Table 4.4: Charge-transfer resistance values extracted from EIS measurements.

4.8 Photocatalytic Experiments

To test the photocatalytic activity of the photocatalyst samples multiple photocatalytic experiments were conducted that includes varying concentration of dopants in photocatalytic reaction with an additional environemts testing on the pH values influence.

4.8.1 Alkali metal doping

H_2O_2 photosynthesis was carried out in a photocatalytic reactor. Initially, the impact of varying potassium ion doping on photocatalytic H_2O_2 production was investigated. It was chosen to increase the concentration of dopant with of 0.25, 0.75, 1.25, and 2.50 mmol. As seen on the Figure 4.16, then the photocatalytic H_2O_2 yield increase over time reaching the highest concentration after 240 min. Similar the increasing concentration of dopant also causes the H_2O_2 yield to increase up to 1.25 mmol after which it decline at 2.50 mmol, which could be attributed to formation of recombination centers [22]. All samples shows approximately the same increase in H_2O_2 concentration with irradiation time, indicating a continuous generation of H_2O_2 during the photocatalytic reaction. Although, it should be noted that as H_2O_2 also decomposes due to its instability, see 2.3.5. Therefore, the yield isn't linear over time, which is partly the reason why the data presented as a column plot.

Compared to the pristine PCN sample, then all potassium doped samples exhibited enhanced photocatalytic activity, suggesting that the presence of K^+ ions contributes positively to the formation of H_2O_2. The sample with 1.25 mmol K showed the highest yield, reaching 62.27 mg/L after 240 min of irradiation. This corresponds to more than 4-times the concentration of Pristine PCN sample, which reached 14.5 mg/L after 240 min. This enhancement with increasing K loads up to the optimal loading can be attributed to improved charge separation and charge transport.

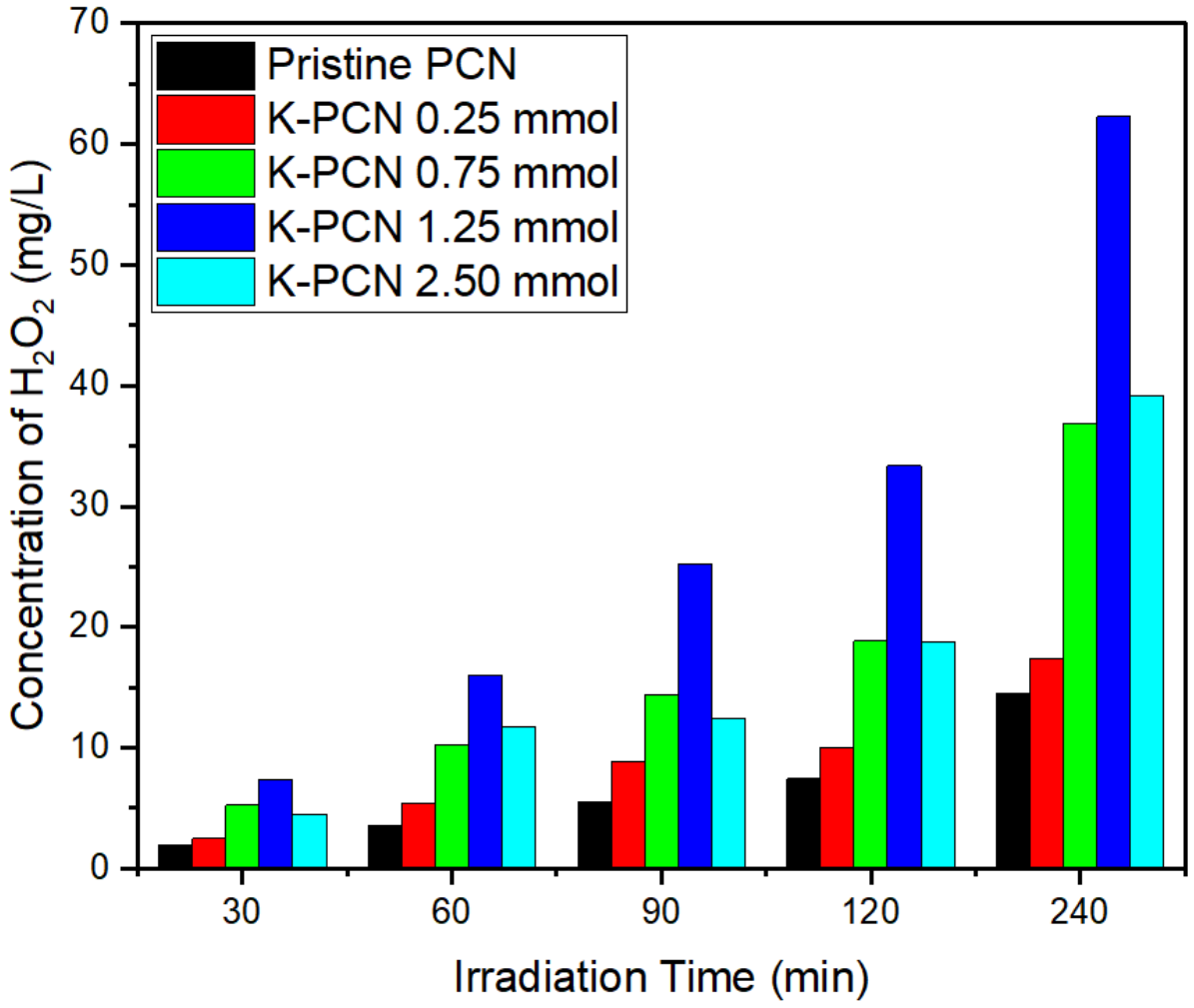

Figure 4.16: Amounts of H_2O_2 produced from K-PCN

4.8.2 d^{10} element doping

To find the second metal for co-doping, then different elements were tested, which includes Sb, Sn, Te, and In. The precursors viable were SbCl3, SnCl2, TeCl4, and InCl3. They were tested at a concentration of 2.50 mmol. All samples exhibit a steady increase in H_2O_2 concentration over time, indicating continuous photocatalytic activity during the irradiation period. However, none of the dopants achieved a higher activity after 240 min than Pristine PCN. Therefore, the precursor $NaSbF_6$ was tested instead for Sb as it is found to have a positive effect in the Study [11]. Using this new precursor with the same concentration of 0.25 mmol, the doping showed an enhancement in the H_2O_2 production reaching 14.6 mg/L after 240 min, which is a slight improvement from the Pristine PCN at 14.5 mg/L. The superior performance of Sb can be attributed to its ability to improve charge carrier separation by the formation of mid-gap states and extend the visible light absorption. Based on these results, Sb was selected as the optimal metal dopant for further experiments involving variation in Sb concentration to further optimize photocatalytic performance.

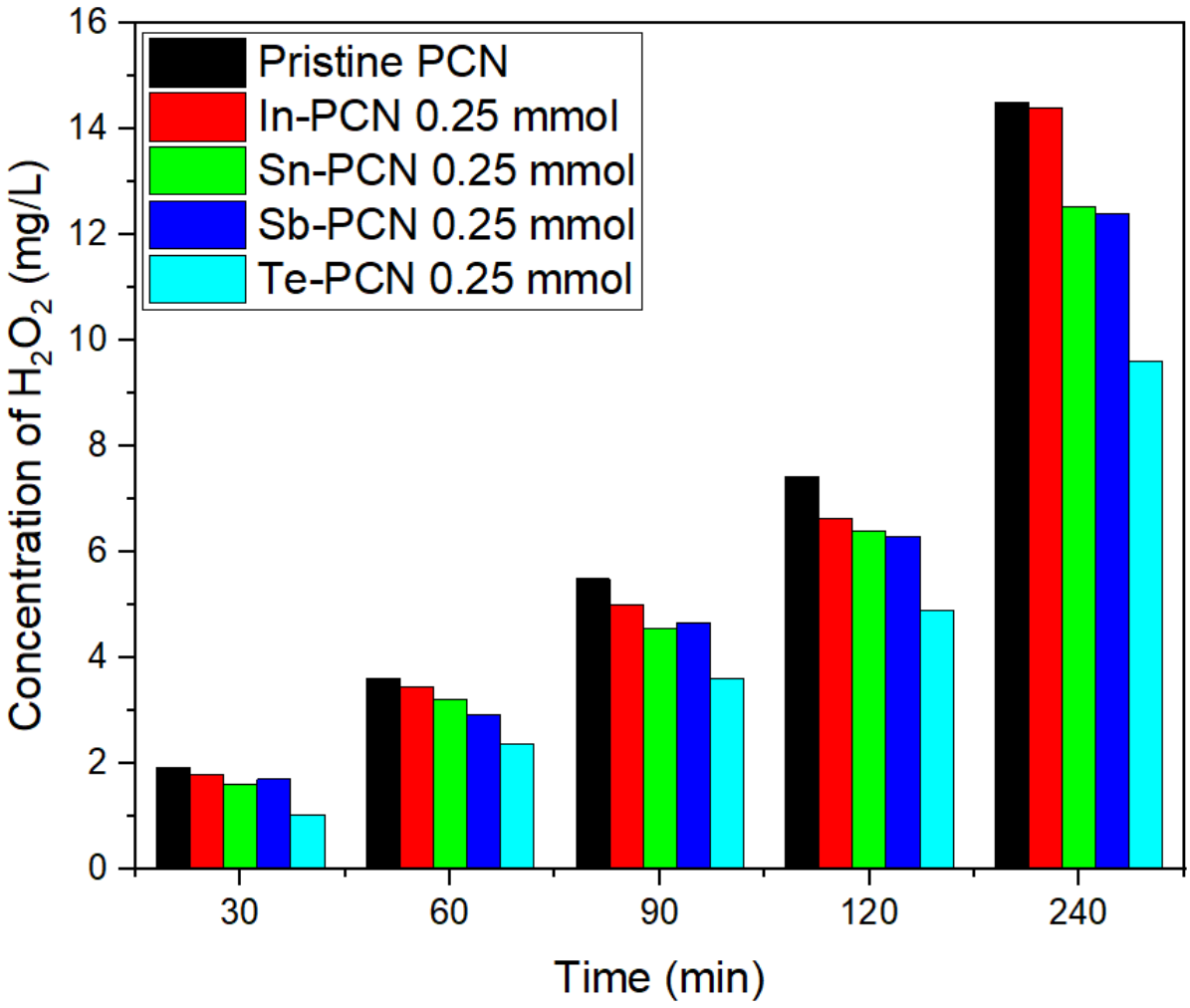

Figure 4.17: Amounts of H_2O_2 produced from different metals

4.8.3 Antimony doping

The effect of Sb doping on photocatalytic H_2O_2 production was investigated to identify the optimal Sb concentration. Figure 4.18 shows the H_2O_2 yield for Pristine PCN and Sb-doped samples with Sb loadings ranging from 0.25 to 5.00 mmol. All Sb-doped samples exhibit higher H_2O_2 concentrations after 240 min compared to Pristine PCN, indicating that Sb incorporation enhances charge separation and thereby improves photocatalytic activity. From tested concentrations, then the Sb-PCN 1.25 mmol sample showed the highest H_2O_2 yield of 18.8 mg/L^{-1} up to Sb-PCN 2.50 mmol, after which Sb-PCN 2.50 mmol performes worse than Sb-PCN 1.25 mmol suggesting that excess Sb loading may introduce recombination centers that decreases activity.

At even higher concentrations, then the samples containing 3.75 and 5.00 mmol Sb showed higher H_2O_2 concentrations after 240 min. However, their activity is shown to only increase a lot more after 120 min. Therefore, it was noted that this was a possible secondary effect from excess Sb2O3, as Sb3O3 peaks appear for XRD 4.1 for specific Sb-PCN 3.75 and Sb-PCN 5.00 mmol. Due to lower both lower

initial H_2O_2 yield up to 120 min and that there have already been observed a decline in activity at 2.50 mmol, then 1.25 mmol Sb sample was selected as the optimal Sb loading for further photocatalytic studies involving combined potassium and antimony co-doping as it was the most consistent and stable performance with high photocatalytic activity.

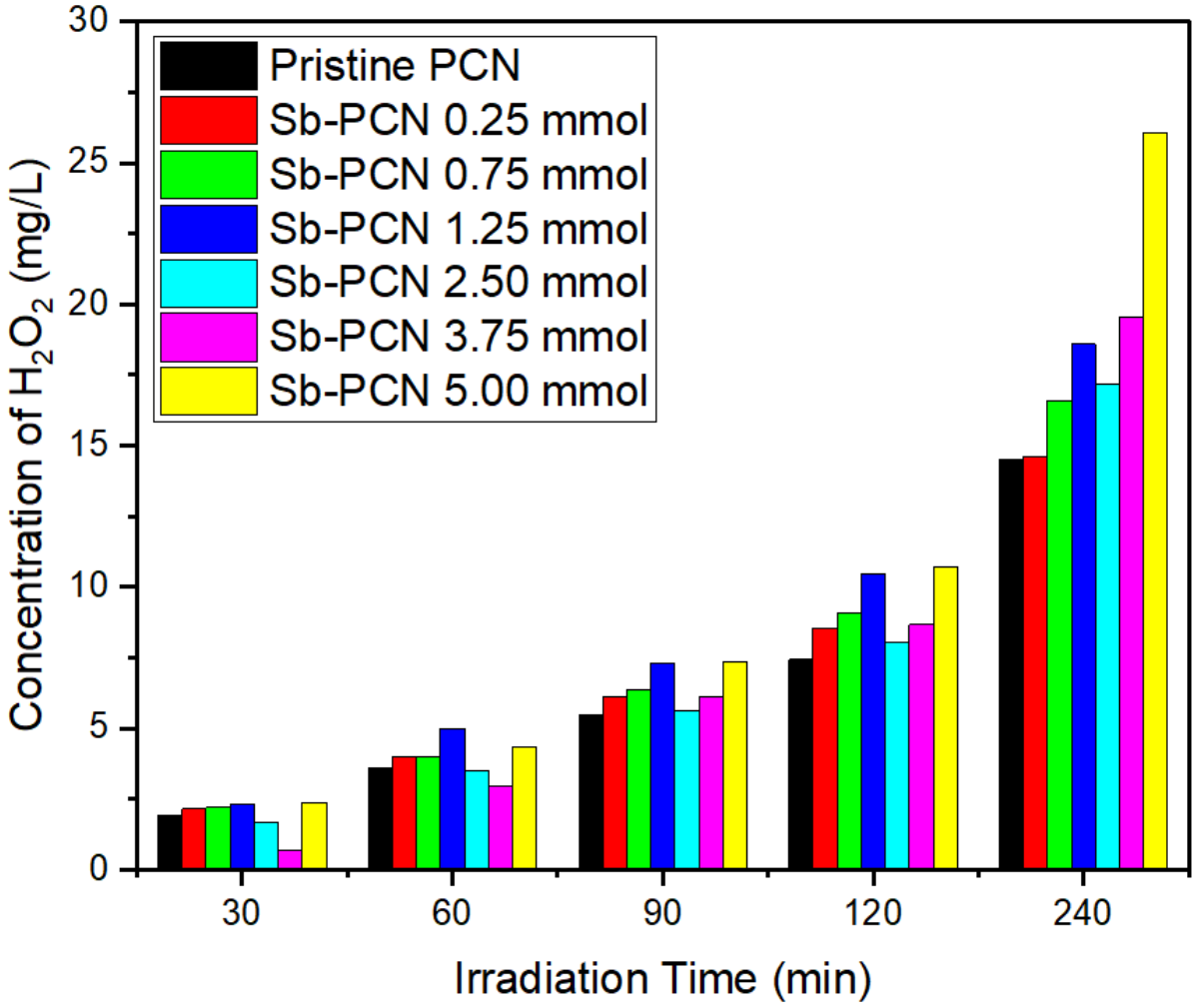

Figure 4.18: Amounts of H_2O_2 produced from Sb-PCN

4.8.4 Co-doping of Antimony and Potassium

The photocatalytic performance of the potassium–antimony co-doped samples was evaluated to examine the combined effect of both dopants. Figure 4.19 shows the H_2O_2 production of the Sb–K-PCN samples with the ratios of 10:1, 10:3, and 10:5. All co-doped samples exhibit higher photocatalytic activity than Pristine PCN throughout the entire irradiation period, confirming that the simultaneous incorporation of Sb and K improves the photocatalytic performance relative to Pristine PCN.

With increasing K content, the photocatalytic activity progressively increases, with the Sb–K (10:5) sample achieving the highest H_2O_2 yield after 240 min. Interestingly, the Sb–K (10:1) sample performs slightly worse than the singly doped 1.25 mmol Sb sample, indicating that the introduction of a small

amount of K can initially disrupt the favorable charge-separation effects provided by Sb. However, at higher K contents (10:3 and 10:5), the activity surpasses that of only Sb doped, demonstrating that both dopants can act cooperatively when their relative concentrations are balanced.

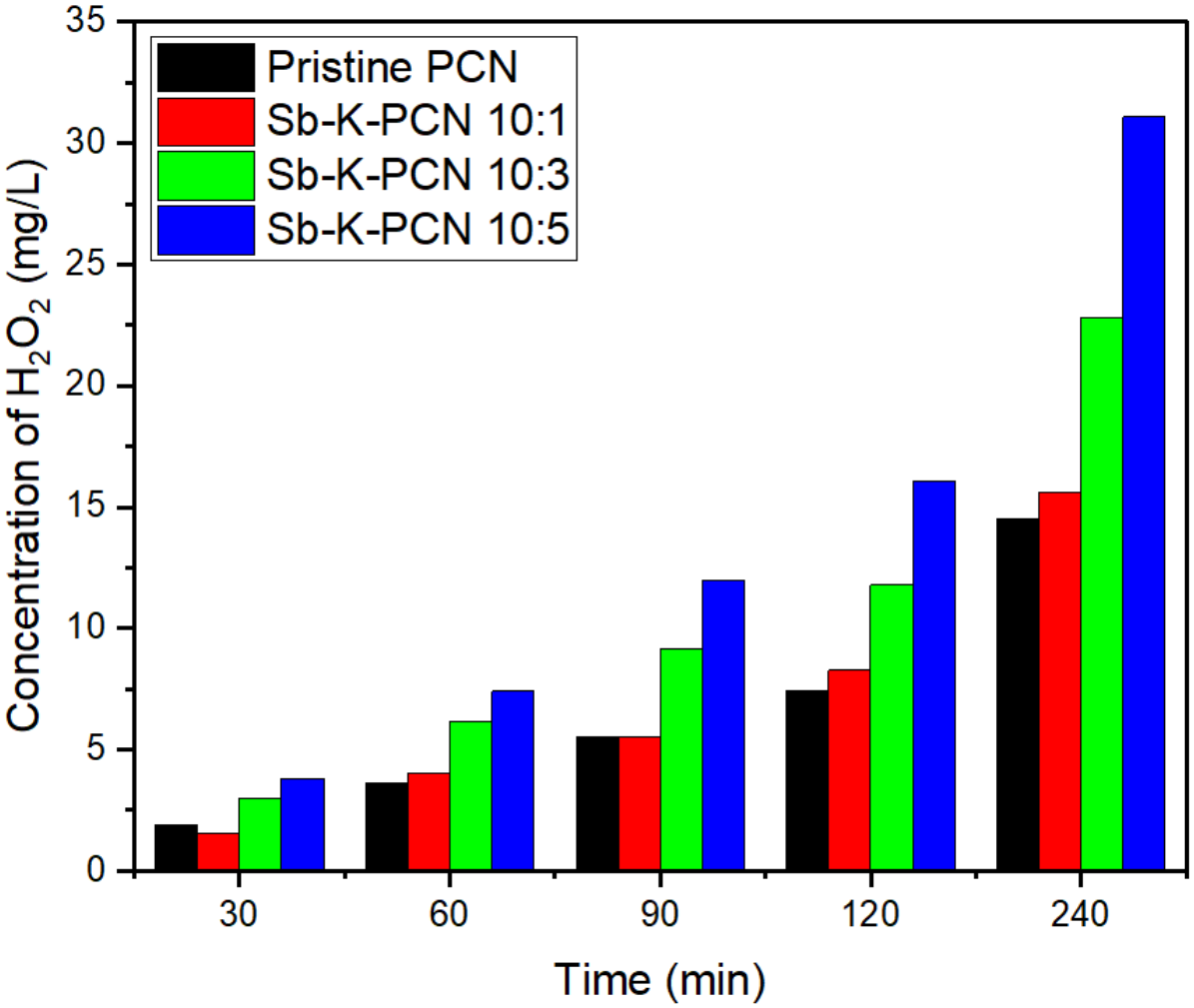

Figure 4.19: Amounts of H_2O_2 produced from Sb-K-PCN

4.8.5 Effect of Acidic and Alkaline Environments

The influence of pH on photocatalytic H_2O_2 production was investigated for Sb–K–PCN (10:3) and Sb–PCN (1.25 mmol) after 240 min of irradiation, and the results are presented in Figure 4.20.

For Sb–K–PCN (10:3), the H_2O_2 concentration decreases as the pH increases from acidic to alkaline conditions. The concentration decreases from 11.3 mg L^{-1} at pH 4 to 9.8 mg L^{-1} at pH 10. This moderate decline indicates that the photocatalyst maintains activity over a relatively wide pH range, although alkaline conditions slightly suppress H_2O_2 production. This suppression can be attributed to the reduced availability of protons required for the oxygen reduction reaction (ORR) and the accelerated decomposition of H_2O_2 in basic media, see Section 2.1.

A similar but more pronounced trend is observed for Sb–PCN (1.25 mmol). At pH 4, the sample produces 31.3 mg L^{-1} of H_2O_2, while increasing the pH to 10 results in a lower concentration of 19.7 mg L^{-1}. This stronger pH dependence suggests that Sb–PCN benefits more from acidic conditions, consistent with the proton-coupled nature of the ORR pathway. The reduced performance under alkaline conditions is further associated with the decreased stability of H_2O_2 at higher pH.

When the reaction was carried out under near-neutral conditions (pH $\sim$ 7) without the addition of HCl or NaOH, the two catalysts exhibited different behaviors. Sb–K–PCN (10:3) achieved a H_2O_2 concentration of 22.8 mg L^{-1}, which is higher than its performance under both acidic and alkaline conditions. In contrast, Sb–PCN (1.25 mmol) produced 18.6 mg L^{-1} at pH $\sim$ 7, which is lower than its yield under acidic conditions but comparable to that obtained at pH 10. These results indicate that Sb–K–PCN exhibits improved activity in neutral conditions, whereas Sb–PCN remains more favorable in acidic environments. A reason for this, could be that Sb–K–PCN compared to Sb–PCN is partly reliable on K^+, which is located in the inter-plane, where it interact more with the environement. This could render the photocatalyst more sensitive to changes in the reaction environment. Variations in the pH could affect the proton availability, surface charge, and the stability of H_2O_2, leading to more pronounced performance fluctuations upon the addition of HCl or NaOH. Therefore, a near-neutral pH provides a balanced environment in which efficient H_2O_2 generation and suppressed decomposition are achieved for Sb–K–PCN.

This highlight the importance of the environment for photocatalytic H_2O_2 production. Acidic conditions generally favor higher yields due to enhanced ORR kinetics, while alkaline conditions promote H_2O_2 decomposition. Co-doping with Sb and K broadens the effective pH window, improving photocatalytic performance under near-neutral conditions.

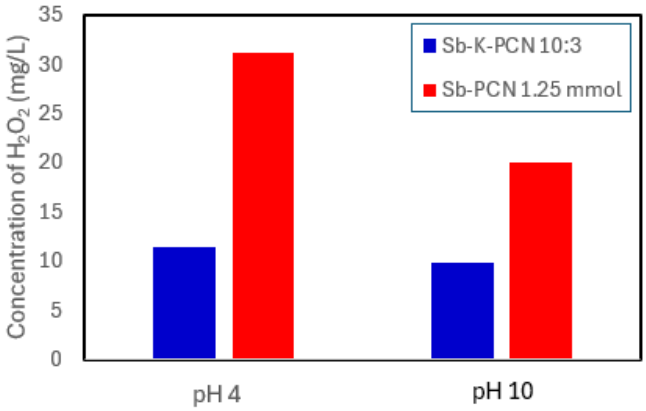

Figure 4.20: Amounts of H_2O_2 produced from Sb-PCN 1.25 mmol and Sb-K-PCN 10:3 at pH=4 and pH=10

4.9 Choice of precursor

The choice of antimony precursor has shown to have a big influence on both the structure and photocatalytic activity of the doped PCN materials. In the case of $NaSbF_6$, the precursor is incorporated

into melamine to form a Sb melamine intermediate, and the fluoride can be fully removed only at sufficiently high temperature. As demonstrated in the Study, [27], calcination at 520 °C leaves residual F in the PCN framework, which prevents complete polymerization of the graphitic carbon nitride and results in inferior photocatalytic activity. Only heating to 560 °C enables full F removal and proper network formation.

A similar limitation explains the poor performance of samples prepared from $SbCl_3$. KCl cannot be volatilized or removed at 560 °C, and therefore residual some KCl still remains in the sample. This trapped KCl disrupts the polymerization of the heptazin6e units, suppresses the formation of an extended π-conjugated network, and introduces structural defects, supported by the XRD for Figure 4.21 that shows decrease in crystallinity from 0.25 mmol to 2.50 mmol for Sb-doped PCN using a SbCl3 precursor. Consequently, using the $SbCl_3$ in the attempt to dope PCN will significantly lower photocatalytic activity compared to those prepared from NaSbF6 precursors. The behaviour of the disruption from residue precursor is fully consistent with the mechanism observed for fluoride at insufficient calcination temperature for the Study, [27], when the halide cannot be removed during thermal condensation, the graphitic carbon nitride framework cannot form properly, leading directly to worse photocatalytic performance. Additionally, it was also found as previously mentioned in this study [26] that using KCl as a dopant requires a extra washing and drying step to remove residues. Lastly, Figure 4.1 also shows that PCN peaks are completely gone and newly formed KCl peaks remaining at the highest KCl concentration.

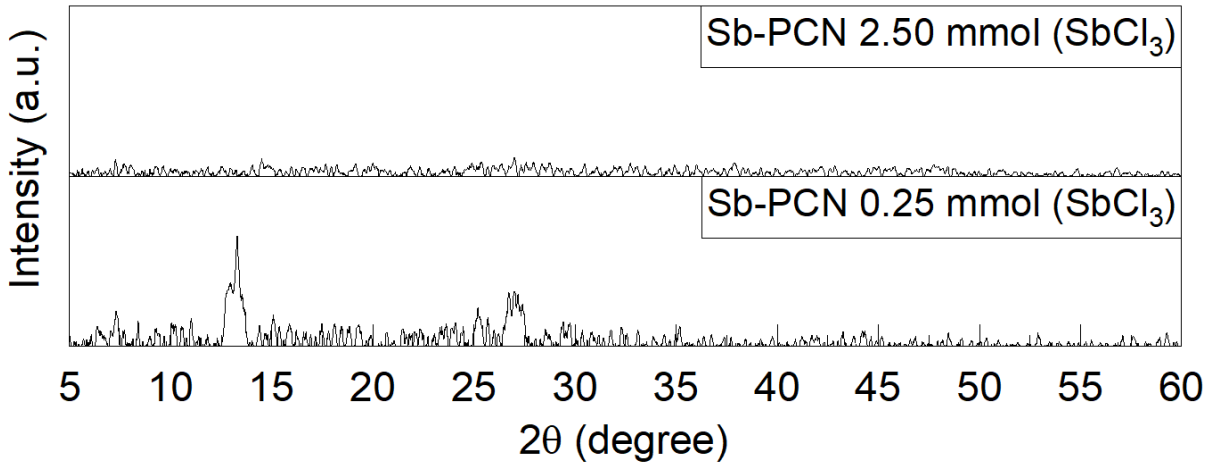

Figure 4.21: XRD of Sb-PCN 0.25 mmol using the precursor $SbCl_3$.

4.10 EPR

EPR spectroscopy was performed for the Sb–K–PCN 10:3 sample to identify the reactive oxygen species generated during photocatalytic H_2O_2 formation. The measurements were carried out under dark and light irradiation using DMPO as the spin-trapping agent and TEMPO was used as a spin probe for photogenerated holes (h^+) (Figure 4.22).

In the dark, no detectable signals corresponding to DMPO–OH or DMPO–O_2^- could be observed, which indicates that neither hydroxyl or superoxide radicals forms without photoexcitation. Upon light

irradiation, both spin-trapped species appear clearly, the DMPO–OH adduct displays its characteristic four-line pattern, while the DMPO–O_2^- adduct shows a strong multi-line hyperfine structure. Their emergence exclusively under illumination demonstrates that these reactive oxygen species are generated through a photoinduced redox process.

In addition to the radical signals, the g-factor of the intrinsic paramagnetic center was evaluated from the spectra. Under dark conditions, the EPR signal is found to be $g \approx 0.193$ and does not show a clear resonance feature; therefore, no reliable g-factor can be extracted from the dark spectrum. Upon illumination, however, a distinct resonance appears at $g \approx 2.0034$. This value is characteristic of unpaired electrons localized in vacancy-related defect states within the π-conjugated framework of carbon nitride. The observed $g \approx 2.003$ is consistent with reports of oxygen or nitrogen vacancy centres, confirming the formation of photoinduced trapped electrons under light irradiation. This photoactivated defect signal further supports the enhanced charge separation and reactive oxygen species generation observed in the photocatalytic system.

Lastly, hole detection using TEMPO revealed a reduction of signal from in dark to light, which indicate the formation of holes.

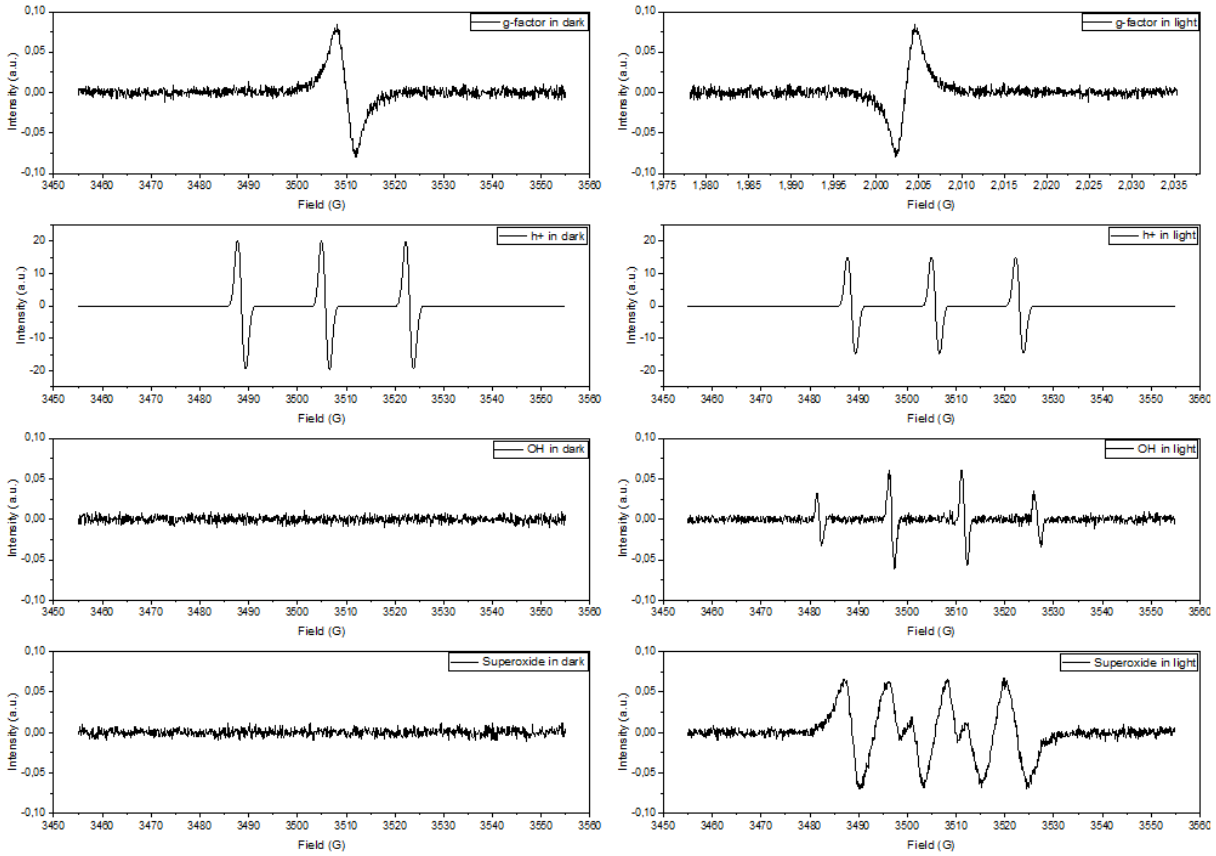

Figure 4.22: EPR spectra of Sb-K-PCN 10:3 recorded under dark and light irradiation using DMPO as a spin-trapping agent and TEMPO was used as a spin probe.

5 | Conclusion

In conclusion, this study demonstrates that targeted doping of PCN with Sb and K is an effective strategy for enhancing photocatalytic H_2O_2 production. Structural characterization using XRD, FT-IR, andXPS confirmed that the fundamental PCN framework is largely preserved after doping, while dopant-induced changes in crystallinity and bonding environments indicate successful incorporation of Sb and K.

Sb was shown to interact directly with the PCN framework through Sb–N and Sb–O coordination, suggesting chemical bonding with nitrogen sites in the network. In contrast, K was primarily present as interlayer K^+ species, where it influences the structure through electrostatic interactions and modification of interlayer charge transport. Optical characterization revealed that both Sb and K doping induce a redshift in the absorption edge and reduce the bandgap of PCN, thereby enhancing visible-light absorption. Sb doping resulted in the most pronounced bandgap narrowing, consistent with the introduction of dopant-related mid-gap electronic states.

PL and TRPL measurements demonstrated suppressed charge recombination and prolonged charge-carrier lifetimes in doped samples, indicating more efficient charge-carrier. EIS further showed that doped PCN exhibits reduced charge-transfer resistance compared to pristine PCN. In particular, K-doped samples displayed low charge-transfer resistance due to enhanced interlayer charge transport, in agreement with theoretical expectations. Co-doping with Sb and K revealed that relatively low K concentrations are sufficient to significantly improve the charge-transfer properties of Sb-doped PCN.

Photocatalytic experiments confirmed that both Sb, K, and co-doped doping enhance H_2O_2 production, with an optimal loading of 1.25 mmol for both dopants. Furthermore, pH-dependent studies showed that acidic and near-neutral environments favor H_2O_2 production, whereas alkaline conditions suppress activity due to reduced proton availability and accelerated oxidative decomposition of H_2O_2. This study demonstrates that d^{10} element and alkali metals can be used to tune the electronic structure and charge-carrier dynamics of PCN, leading to enhanced photocatalytic H_2O_2 production. These findings highlight the potential of doped PCN as a greener and more sustainable alternative for future hydrogen peroxide production.

6 Further work

While this study demonstrates that antimony (Sb) and potassium (K) doping can effectively enhance the photocatalytic activity of PCN for H_2O_2 generation, several aspects warrant further investigation. Future work should first focus on optimizing the synthesis procedure to minimize the presence of residues, such as KCl. Additional washing steps or the use of alternative potassium precursors could help separate the effects of K doping have from residual salt.

Further insight into the structural effects of dopant incorporation could be obtained through scanning electron microscopy (SEM), which would provide more detailed information on morphology, particle size, and dopant distribution within the PCN framework. Such analysis could complement the existing structural characterization and contribute to a more complete understanding of dopant-induced structural impact.

The photocatalytic mechanism could be explored in greater depth through density functional theory (DFT) calculations, which would complement the experimental findings with theoretical insight. In particular, DFT studies could show how Sb and K induced electronic states influence the band structure, charge separation, and charge-transfer pathways involved in the ORR.

Then there should also be investigated further into d10-element dopants at higher loadings and using different precursors could help establish general design principles for optimizing PCN-based photocatalysts. Although this study initially aimed partly to explore a broader range of d10 elements, then this was limited by time. Exploring different elements could help identify alternative dopants with comparable or superior performance.

Finally, future studies should also address the long-term stability and scalability of doped PCN photocatalysts. Testing the catalyst durability over extended reaction times and assessing performance under conditions closer to real-world operation would be essential to determine whether doped PCN systems have the potential to transition from laboratory-scale research to practical applications.

Bibliography

[1] Jingbo Ni, Vittorio Boffa, Xiaoyu Sun, Teruhisa Ohno, Lorenzo Sarasino, Maria Cristina Paganini, and Paola Calza. Self-assembly synthesis of gallium-doped polymeric carbon nitride/Ti3C2 MXene Schottky junction for efficient photosynthesis of hydrogen peroxide. *Applied Surface Science*, 704, 9 2025.

[2] Xingyi Shi, Yuran Bai, Xiaoyu Huo, Yun Liu, Lizhen Wu, Wenzhi Li, Qixing Wu, and Liang An. Performance Characteristics of a H2O2-Based Fuel Cell under Extreme Environments. *Energy and Fuels*, 38(20):19860–19866, 10 2024.

[3] Greg Sharp. Catalytic Oxidation Reactions Using Hydrogen Peroxide. Technical report, 2023.

[4] Jacob Bronowski. *Verden omkring os: Naturens kræfter*. Gyldendal, København, 7 1961.

[5] Jose M. Campos-Martin, Gema Blanco-Brieva, and Jose L.G. Fierro. Hydrogen peroxide synthesis: An outlook beyond the anthraquinone process, 10 2006.

[6] Stefano Lettieri, Michele Pavone, Ambra Fioravanti, Luigi Santamaria Amato, and Pasqualino Maddalena. Charge carrier processes and optical properties in TiO2 and TiO2-based heterojunction photocatalysts: A review. *Materials*, 14(7), 3 2021.

[7] Shibo Shao, Xiangzhou Wang, Wenbing Li, Yiming Zhang, Shi Liu, Weisheng Xiao, Zongyang Yue, Xu Lu, and Xianfeng Fan. A mini review on photocatalytic lignin conversion into monomeric aromatic compounds, 1 2025.

[8] Sin Ki Lai, Chao Xie, Kar Seng Teng, Yanyong Li, Furui Tan, Feng Yan, and Shu Ping Lau. Polymeric Carbon Nitride Nanosheets/Graphene Hybrid Phototransistors with High Responsivity. *Advanced Optical Materials*, 4(4):555–561, 4 2016.

[9] Gege Zhao, Bangwang Li, Xiaonan Yang, Xiaomeng Zhang, Zhongfei Li, Daochuan Jiang, Haiwei Du, Chuhong Zhu, Huiquan Li, Can Xue, and Yupeng Yuan. Two birds with one stone: Engineering polymeric carbon nitride with n-π electronic transition for extending light absorption and reducing charge recombination. *Advanced Powder Materials*, 2(1), 1 2023.

[10] Vincent Wing Hei Lau, Igor Moudrakovski, Tiago Botari, Simon Weinberger, Maria B. Mesch, Viola Duppel, Jürgen Senker, Volker Blum, and Bettina V. Lotsch. Rational design of carbon nitride photocatalysts by identification of cyanamide defects as catalytically relevant sites. *Nature Communications*, 7, 7 2016.

[11] Zhenyuan Teng, Qitao Zhang, Hongbin Yang, Kosaku Kato, Wenjuan Yang, Ying Rui Lu, Sixiao Liu, Chengyin Wang, Akira Yamakata, Chenliang Su, Bin Liu, and Teruhisa Ohno. 1 Atomically dispersed antimony on carbon nitride for the artificial photosynthesis of hydrogen peroxide. *Nature Catalysis*, 4(5):374–384, 5 2021.

[12] Huagen Liang, Haoran Wang, Anhu Wang, Ruolin Cheng, Shengyu Jing, Fu Chen, Palanisamy Kannan, Georgia Balkourani, and Panagiotis Tsiakaras. Efficient photocatalytic hydrogen peroxide production over S-scheme In2S3/molten salt modified C3N5 heterojunction. *Journal of Colloid and Interface Science*, 669:506–517, 9 2024.

[13] Ioannis Papagiannis, Nikolaos Balis, Vassilios Dracopoulos, and Panagiotis Lianos. Photoelectrocatalytic hydrogen peroxide production using nanoparticulate WO3 as photocatalyst and glycerol or ethanol as sacrificial agents. *Processes*, 8(1), 1 2020.

[14] A. S. Abdel-Rahman and Youssef A. Sabry. A quantum–classical approach band model of indirect optical transitions in semiconductor materials. *Optical and Quantum Electronics*, 58(1):34, 12 2025.

[15] Adhe Aryswan. Hierarchical Porous g-C 3 N 4 as a Photocatalyst Nanomaterial. *Journal of Research and Development on Nanotechnology Review*, 1:1–5, 2021.

[16] Gareth O. Hartley and Natalia Martsinovich. Computational design of graphitic carbon nitride photocatalysts for water splitting. *Faraday Discussions*, 227:341–358, 4 2021.

[17] Muhammad Rizwan, Amir Zada, Shohreh Azizi, Perveen Fazil, Mohammad Naeem, Ghulam Murtaza, Nasir A. Ibrahim, Nosiba Suliman Basher, Zhongchuang Liu, and Mohamed Hassan Eisa. Role of metal and non-metal dopants in modulating g-C3N4 for photocatalytic applications, 1 2025.

[18] Jinbao Chen, Shun Fang, Qun Shen, Jiajie Fan, Qin Li, and Kangle Lv. Recent Advances of Doping and Surface Modifying Carbon Nitride with Characterization Techniques, 9 2022.

[19] Shaymaa N. Ismail, Ehab m. Ali, Bahaa Jawad Alwan, and Ahmed N. Abd. Potassium Chloride Nanoparticles: Synthesis, Characterization, and Study the Antimicrobial Applications. *Macromolecular Symposia*, 401(1), 2 2022.

[20] Yangsen Xu, Xin He, Hong Zhong, David J. Singh, Lijun Zhang, and Ruihu Wang. Solid salt confinement effect: An effective strategy to fabricate high crystalline polymer carbon nitride for enhanced photocatalytic hydrogen evolution. *Applied Catalysis B: Environmental*, 246:349–355, 6 2019.

[21] Y. P. Shinde, P. N. Sonone, R. K. Kendale, P. M. Koinkar, and A. U. Ubale. Growth of hexagonal shape nanostructured Sb2O3 thin films by spray pyrolysis and their structural, morphological, electrical and optical properties. *Journal of Materials Science: Materials in Electronics*, 31(20):17432–17439, 10 2020.

[22] Motahare S. Mohseni-Salehi, Ehsan Taheri-Nassaj, and Maryam Hosseini-Zori. Effect of dopant (Co, Ni) concentration and hydroxyapatite compositing on photocatalytic activity of titania towards dye degradation. *Journal of Photochemistry and Photobiology A: Chemistry*, 356:57–70, 4 2018.

[23] Mark Biesinger. X-ray Photoelectron Spectroscopy (XPS) Reference Pages.

[24] Qingxiang Cao, Xuelian Wu, Yunxiao Zhang, Bo Yang, Xiaofen Ma, Jun Song, and Junmin Zhang. Potassium-doped carbon nitride: Highly efficient photoredox catalyst for selective oxygen reduction and arylboronic acid hydroxylation. *Journal of Catalysis*, 414:64–75, 10 2022.

[25] S. Pourali, R. Amrollahi, S. Alamolhoda, and S. M. Masoudpanah. In situ synthesis of ZnO/g-C3N4 based composites for photodegradation of methylene blue under visible light. *Scientific Reports*, 15(1), 12 2025.

[26] Chengyu Peng, Rong Lu, and Anchi Yu. Unravelling the doping effect of potassium ions on structural modulation and photocatalytic activity of graphitic carbon nitride. *RSC Advances*, 13(14):9168–9179, 3 2023.

[27] Zhenyuan Teng, Qitao Zhang, Hongbin Yang, Kosaku Kato, Wenjuan Yang, Ying Rui Lu, Sixiao Liu, Chengyin Wang, Akira Yamakata, Chenliang Su, Bin Liu, and Teruhisa Ohno. 2 Atomically dispersed antimony on carbon nitride for the artificial photosynthesis of hydrogen peroxide. *Nature Catalysis*, 4(5):374–384, 5 2021.

List of Figures

List of Tables

Appendices

A1. Real Experimental Setup

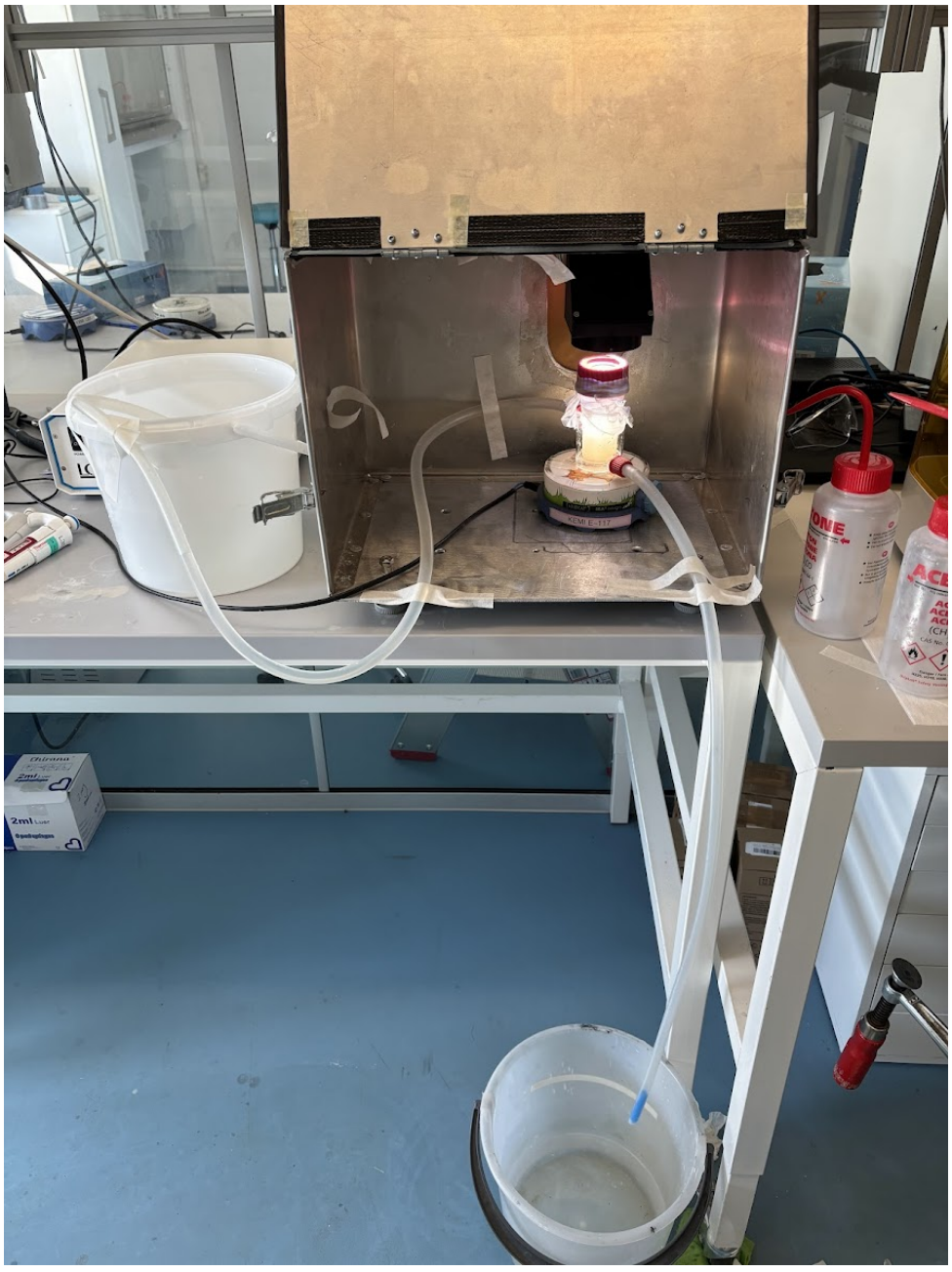

Figure 1: Real experimental setup

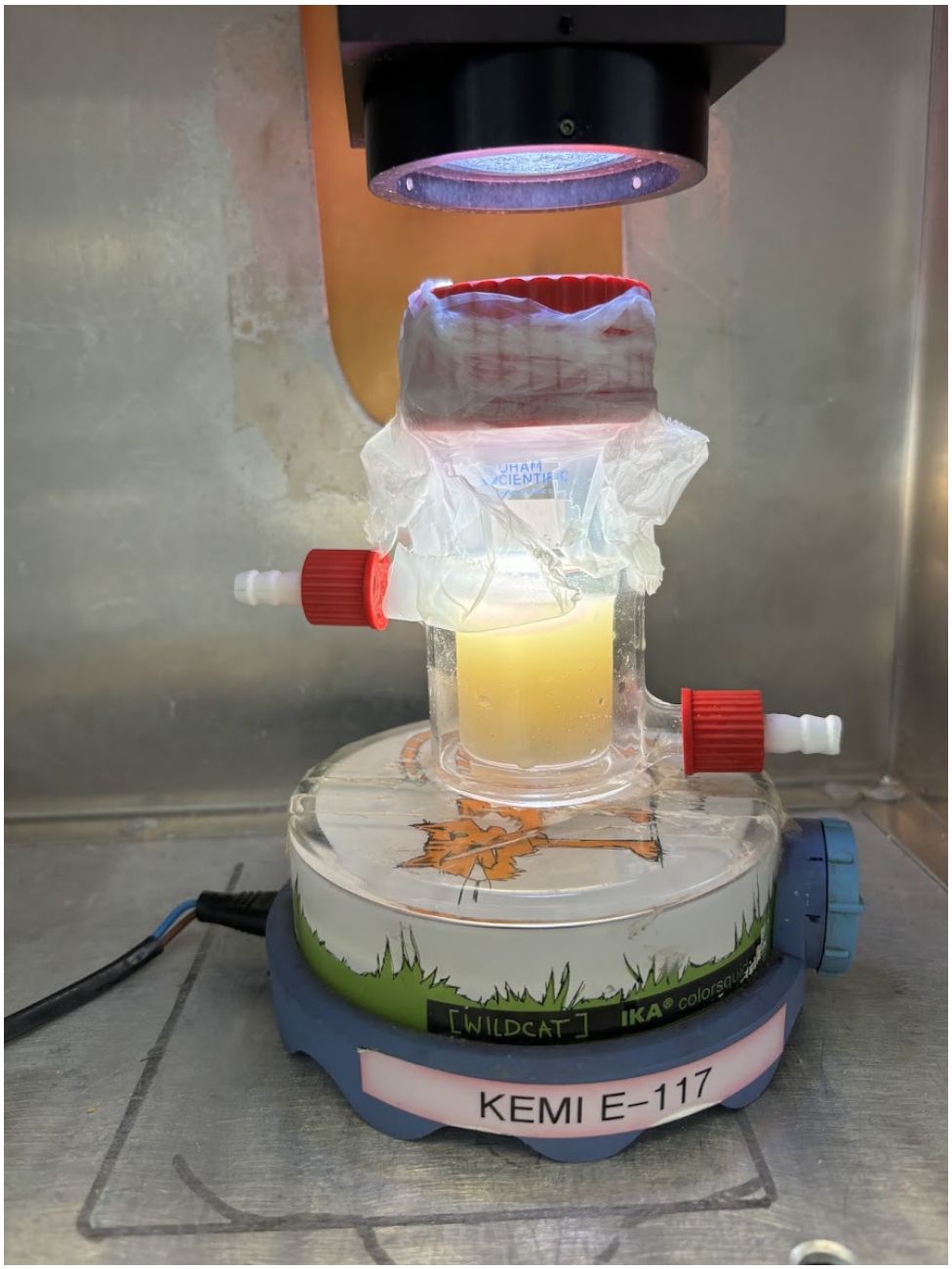

Figure 2: Zoom in of Real experimental setup

A2. Photocatalytic Experiment of additional metal dopants

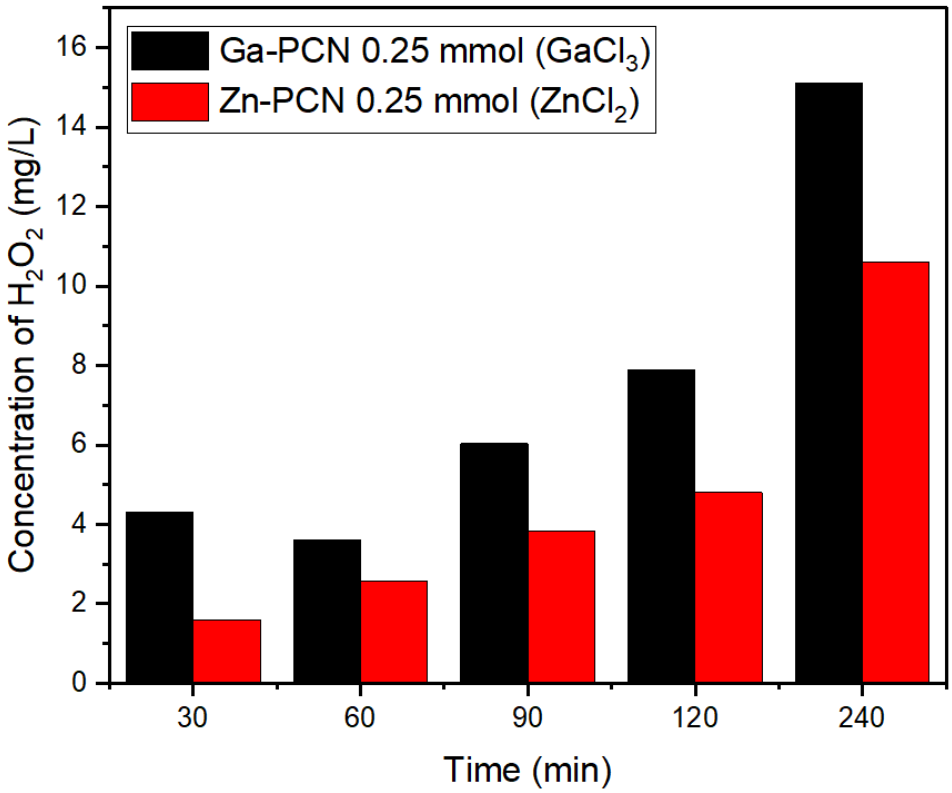

Figure 3: Amounts of H_2O_2 produced from Zn-PCN 0.25 mmol and Ga-PCN 0.25 mmol using $GaCl_3$ and $ZnCl_2$

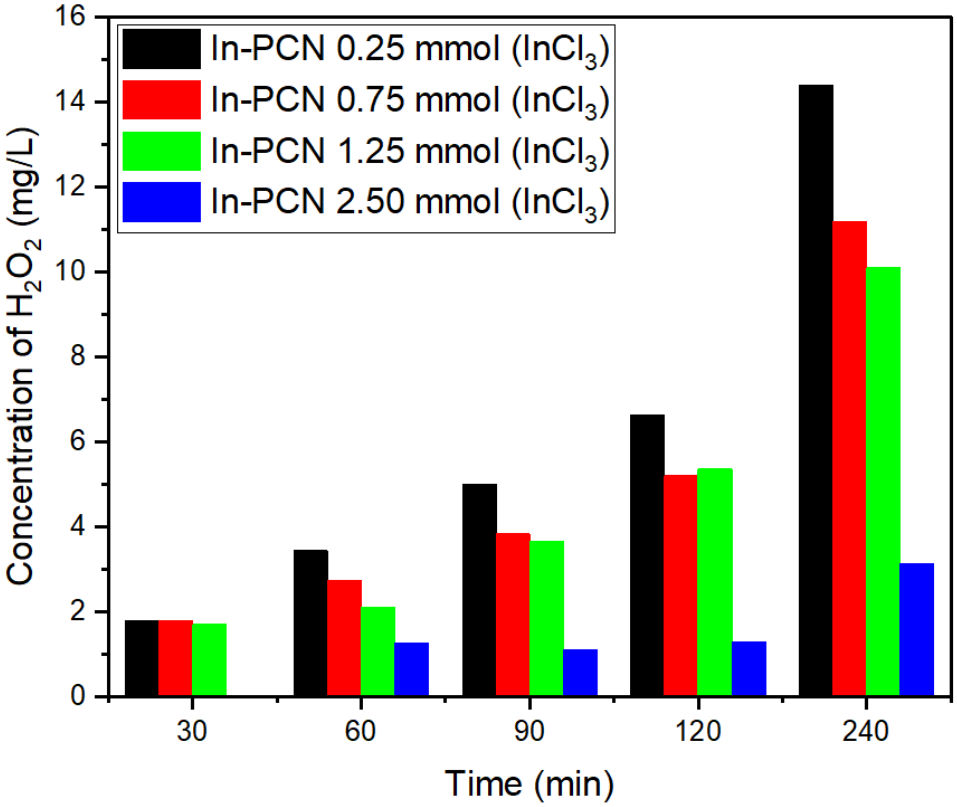

Figure 4: Amounts of H_2O_2 produced from In-PCN using $InCl_3$ ranging from 0.25 mmol to 2.50 mmol

A3. XRD of additional metal-doped PCN

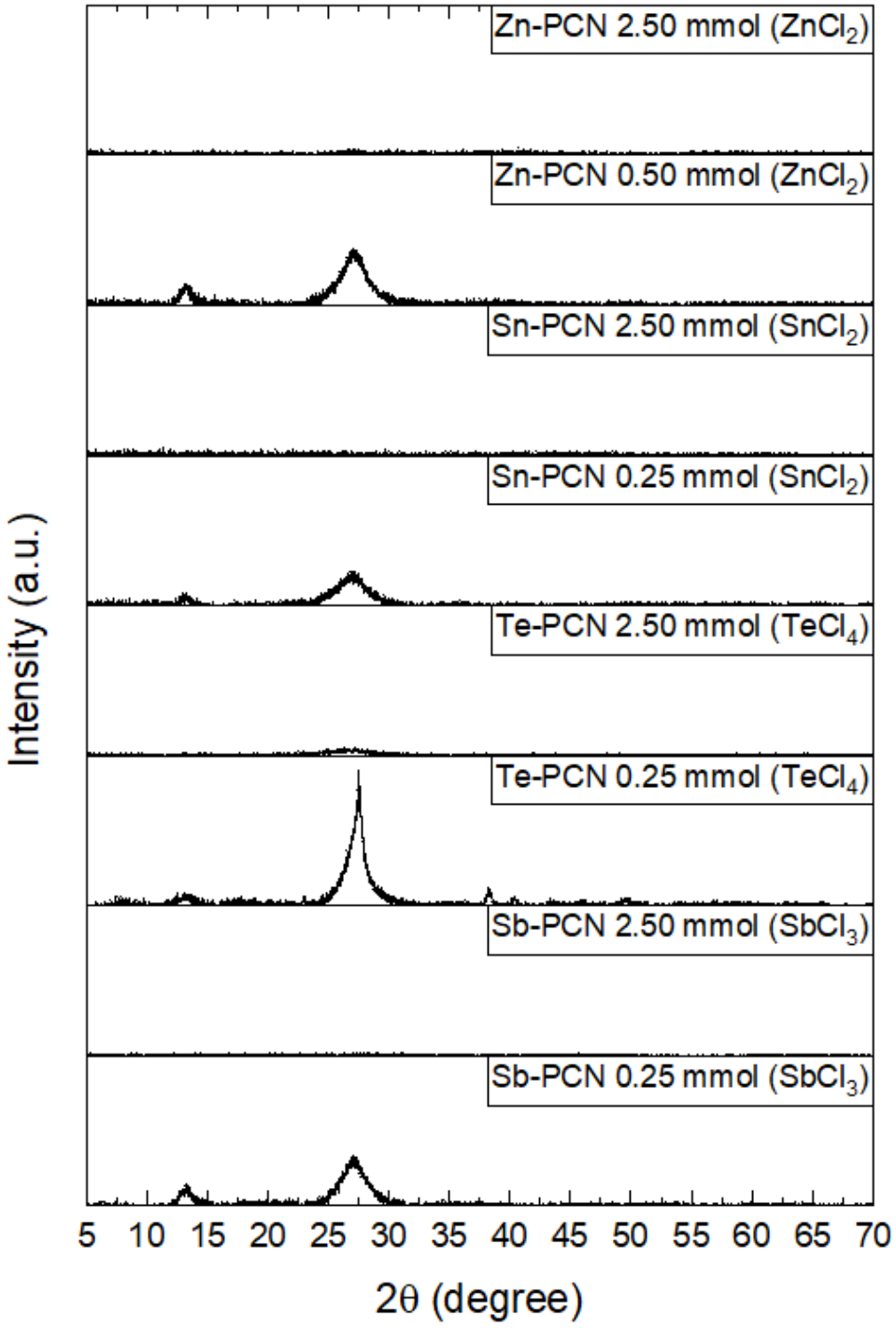

Figure 5: XRD of additional metal-doped PCN

A4. XRD of additional metal-doped PCN

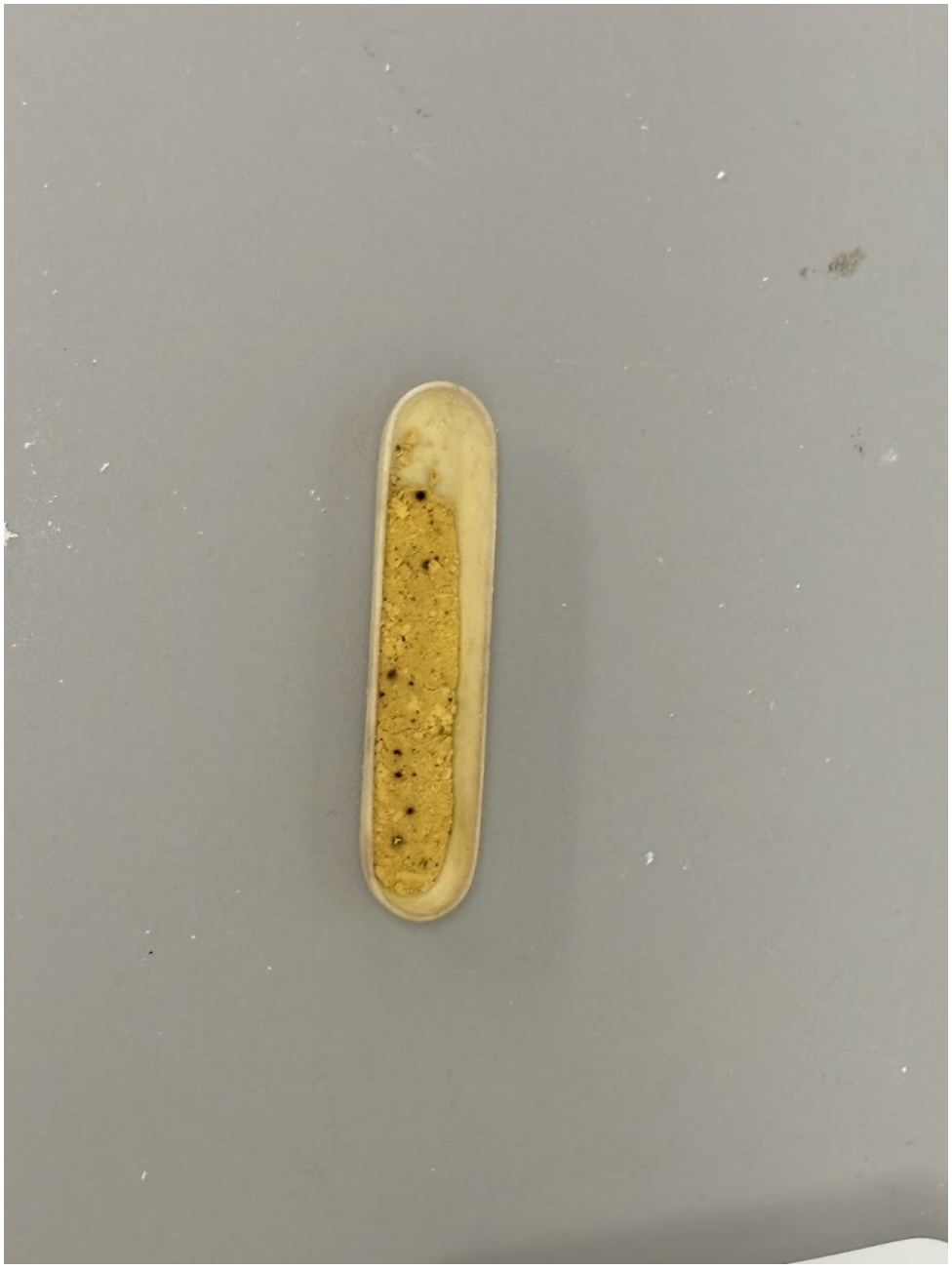

Figure 6: Picture of powder for In-PCN 1.25 mmol sample.

Figure 7: Picture of powder for In-PCN 2.50 mmol sample.

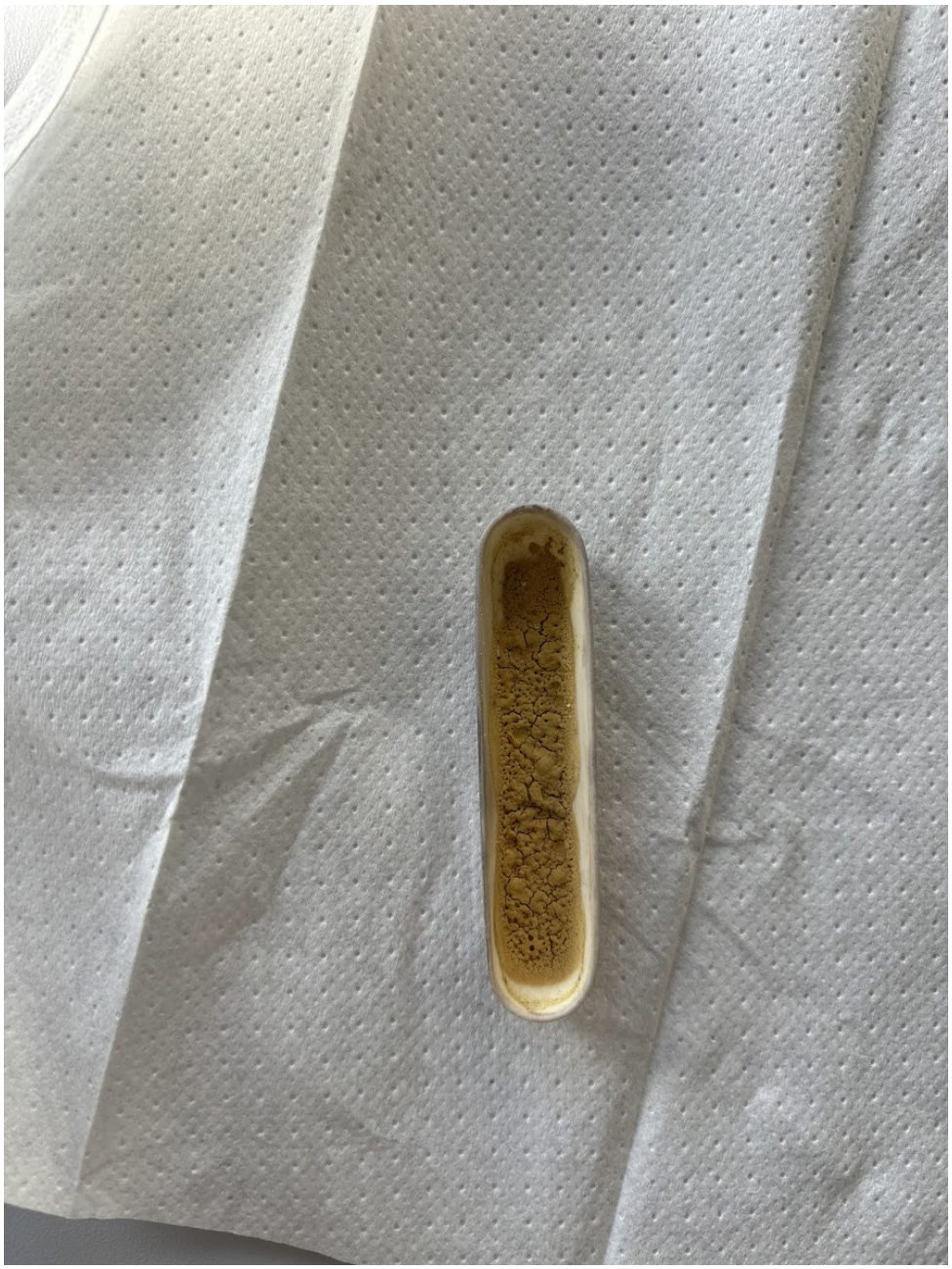

Figure 8: Picture of powder for K-PCN 0.25 mmol sample.

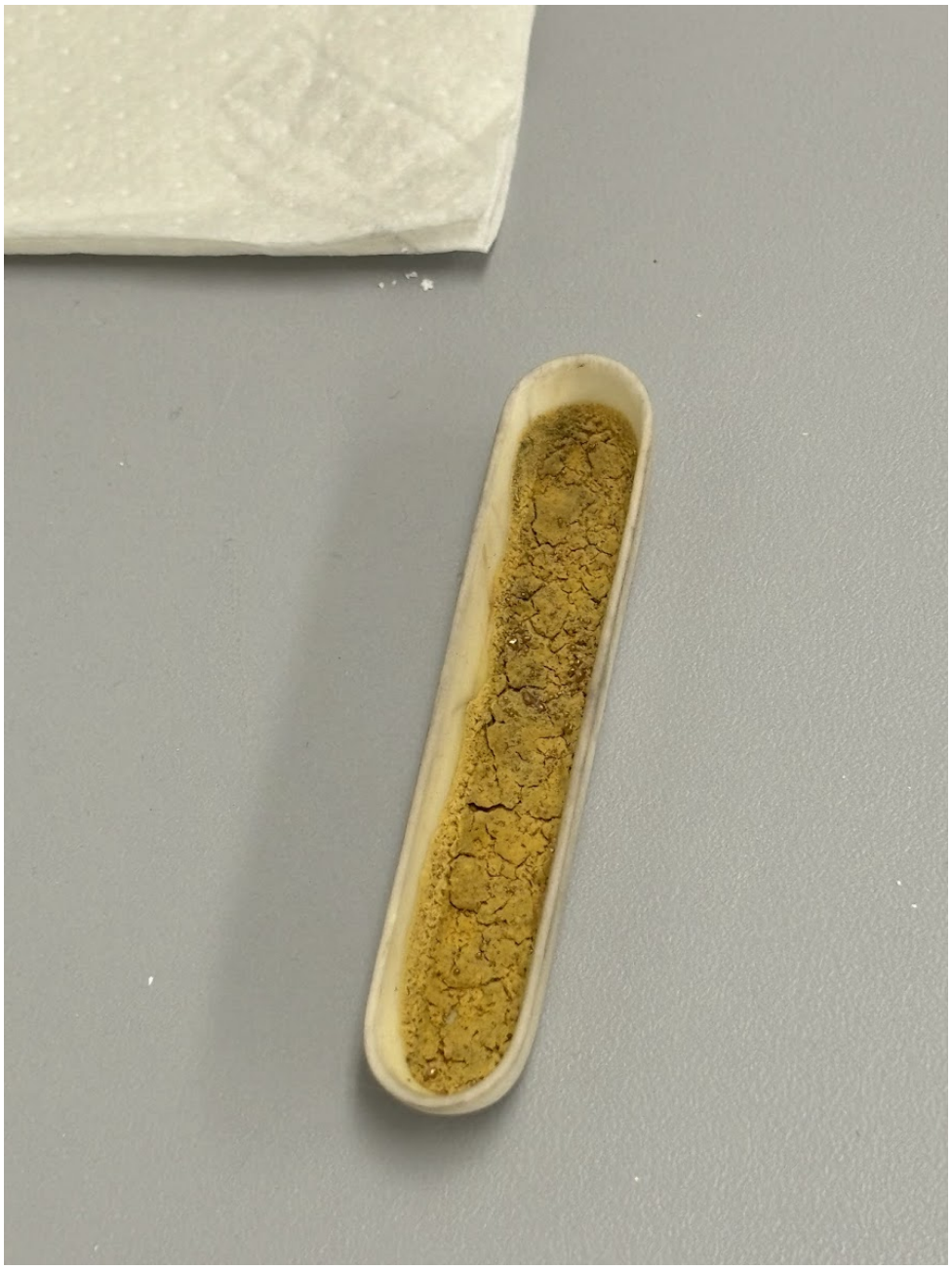

Figure 9: Picture of powder for K-PCN 1.25 mmol sample.

Figure 10: Picture of powder for Sn-PCN 0.25 mmol sample.

Figure 11: Picture of powder for Zn-PCN 0.25 mmol sample.

A5. Instruments

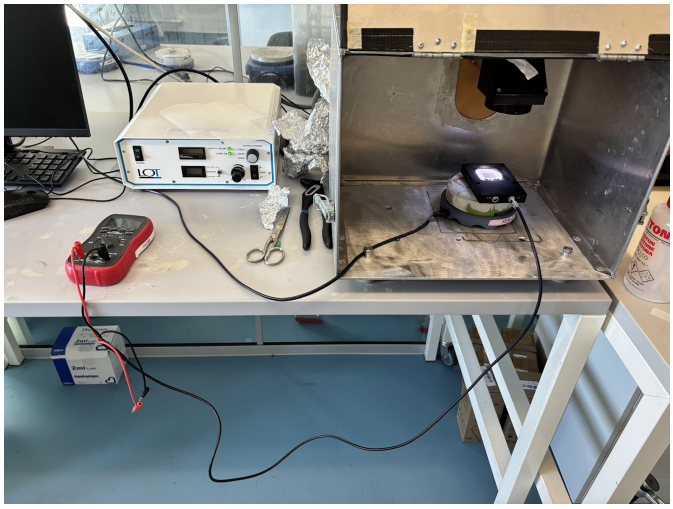

(a) (A)

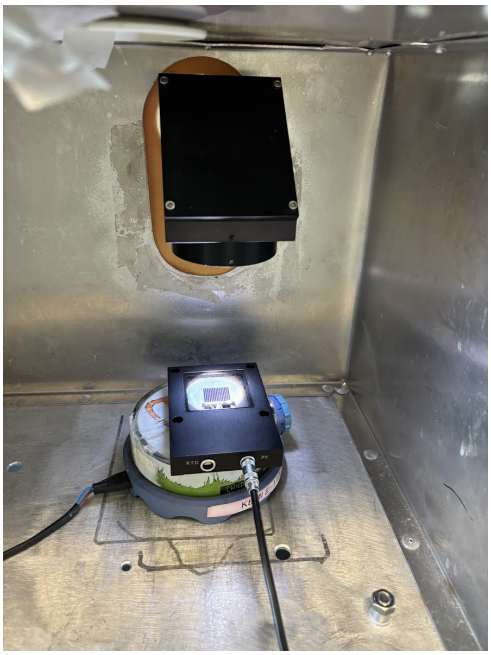

(b) (B)

Figure 12: Solar cell setup (A) and solar cell close up (B)